


RESEARCH ARTICLE

# A transformable wheel-spoke-paddle hybrid amphibious robot

Yikai Ge<sup>1,2</sup>, Feng Gao<sup>1,2</sup> and Weixing Chen<sup>1,2</sup> 

<sup>1</sup>State Key Laboratory of Mechanical System and Vibration, School of Mechanical Engineering, Shanghai Jiao Tong University, Shanghai, 200240, China and <sup>2</sup>Research Center of Marine Intelligent Equipment and Robot, Institute of Marine Equipment, Shanghai Jiao Tong University, Shanghai, China

**Corresponding author:** Weixing Chen; Email: wxchen@sjtu.edu.cn

**Received:** 28 September 2023; **Revised:** 20 November 2023; **Accepted:** 24 November 2023;

**First published online:** 22 December 2023

**Keywords:** amphibious robot; mobile robot; transformable mechanism; multimodal motion

## Abstract

The intricate water-land intermingled nature of wild environments necessitates robots to exhibit multimodal cross-domain mobility capabilities. This paper introduces a novel wheel-spoke-paddle hybrid amphibious robot (WSP-bot) that can operate on flat and rough terrains, water surfaces, and water-land transitional zones. The proposed robot relies on a propulsion mechanism called transformable wheel-spoke-paddle (WSP), which combines the stability of wheeled robots with the obstacle-climbing capability of legged robots, while also providing additional aquatic mobility. The utilization of a crank-slider-based transformation mechanism enables seamless switching between multiple motion modes. An analysis of mode transition and ground motion in spoke mode was conducted, along with an investigation of its obstacle-crossing capability. Simulations were performed for mode transition, ground locomotion, and obstacle-crossing, as well as propulsion of a single WSP module on water. Based on the above work, a prototype robot was manufactured. Prototype tests, including mode transition and mobility tests on land and water surfaces under multimodal states, confirmed the effectiveness of the proposed WSP-bot.

## 1. Introduction

Wild environments of significant exploration value, such as plains, rugged terrains, water bodies, and marshes in transitional water-land areas, demand that robots possess multimodal cross-domain mobility due to complex water-land interweaving nature [1–3]. These robots facilitate the acquisition of valuable scientific data and are capable of effectively executing tasks such as terrain surveys, environmental monitoring, sample collection, search, and rescue [4–6]. However, most conventional mobile robots are designed to handle single land or water terrain, and they tend to struggle in complex environments where land and water are intertwined [7].

As a special type of mobile robot, amphibious robots have great potential for exploration in complex wild environments due to their combined terrestrial and aquatic mobility, which enables them to perform diverse cross-domain tasks [8–10]. The design of propulsion system is crucial for amphibious robots due to their high requirement for cross-domain mobility. Tadakuma et al. [11] developed an amphibious propulsion system called “Omni-Paddle” which features a special spherical omnidirectional wheel with both active and passive rotational degrees of freedom, enabling both terrestrial wheeled movement and aquatic paddling motion. Yu et al. [12, 13] designed AmphiRobot-II, which primarily relies on the active wheel on its head for terrestrial locomotion and utilizes its tail fin and flippers on both sides of the head for stable and efficient fish- or dolphin-like swimming in water. The FroBot designed by Yi et al. [14] utilizes omnidirectional wheels and a pair of flexible flippers resembling frog’s webbed feet to generate propulsion on land and underwater, respectively. Nevertheless, due

to the retention of wheeled features, the above amphibious robots are unable to effectively overcome rough and unstructured terrestrial environments.

Another approach widely welcomed by researchers is the rotating-legged robot, which is developed by removing a portion of the complete wheel rim to form a rotating leg structure [15]. For instance, Boxerbaum et al. [16, 17] developed a cockroach-inspired amphibious robot called “Whegs”, which utilizes a leg-propeller hybrid propulsion system consisting of three propeller-shaped spokes without rims. It exhibits good obstacle-crossing performance on land with the outer edge of its legs contacting the ground, while in water, it propels itself by driving the propeller-shaped legs directly. The RHex robot series utilizes six resilient semi-circular legs for amphibious locomotion, ensuring reliable movement while reducing the number of driving motors [18–22]. Despite exhibiting strong terrain adaptability, it suffers from poor mobility stability. The propulsion mechanism of AQUA is designed to be switchable, using semi-circular legs for movement on land and fins that require manual replacement for water locomotion [23]. Therefore, the subsequent design improvements of the “Ninja legs” aim to integrate the legs and fins directly to achieve free amphibious locomotion without the need for manual replacement of the propulsion mechanism [24]. This type of rotating-legged robot relies on spokes to overcome land obstacles, greatly simplifying the overall structure and control difficulty. However, the incompleteness of the wheel rim results in the fluctuation of the robot’s center of mass (CoM), which negatively impact the stability and speed of land movement.

The aforementioned amphibious robots mostly adopt a direct combination of wheel-paddle/fin or leg-paddle/fin design to achieve amphibious locomotion, which is likely to affect the overall locomotion performance by integrating the propulsion mechanisms used on land and in water into one unit. One possible solution to this issue is to utilize a transformable structure to switch between multiple propulsion modes [25, 26]. Sun et al. [27] developed an eccentric mechanism as the basis to achieve mode switching among wheel, leg, and paddle propulsion by adjusting the eccentric position of the paddles, enabling up to five different gaits. However, the design and control of the propulsion mechanism is complex and challenging. Zhang et al. [28, 29] utilized a leg-fin transformable mechanism driven by steel wires, which enables the supporting legs to switch between semi-circular legs on land and fins in water, but its reliability needs further improvement and it lacks the stability of wheeled locomotion on land. Inspired by the RHex, Ma et al. [30] designed the SHOALBOT, which achieves flexible running on complex terrain and swimming in water by combining propeller legs with body transformation ability. Due to the adopted body transformation mechanism, the overall size of the robot is relatively large and weighs up to 22 kg.

Although the introduction of a transformable mechanism can effectively switch between several modes of movement to meet propulsion requirements in different terrestrial and aquatic environments, there are still some urgent issues to be addressed. Firstly, the designs of transformable mechanisms in current amphibious robots are generally complex, resulting in a large overall mass and high control difficulty, which is unfavorable for compact and small-sized implementation. Secondly, research on small transformable amphibious robots is scarce. It remains a challenge to design a simple and efficient transformable mechanism that can be applied to small amphibious robots and simultaneously possess multimodal cross-domain motion capabilities. Lastly, there is limited attention paid to the water-land transition zones. Existing amphibious robots rarely demonstrate the ability to move in complex terrestrial and aquatic environments, as well as in transitional environments such as swamps and wetlands, through the transformable mechanism with reduced complexity.

This paper proposes a novel transformable wheel-spoke-paddle amphibious robot (WSP-bot). The proposed robot divides the traditional wheel into four parts and adopts an axial push-pull transformation mechanism based on the offset crank slider [31, 32], which can change the working modes according to the surrounding environment with compact structure and simple control strategies. The robot can achieve smooth, high-speed, and flexible movement on flat terrain in wheel mode, adapt to rough terrain in spoke mode, and move on water surfaces in paddle mode. The design of the WSP module simultaneously achieves lightweight construction and multimodal motion. Meanwhile, the unfolded fan-shaped spokes establish ample ground contact, enhancing adaptability to water-land transitional areas. Specifically, the main contributions of this paper are as follows:

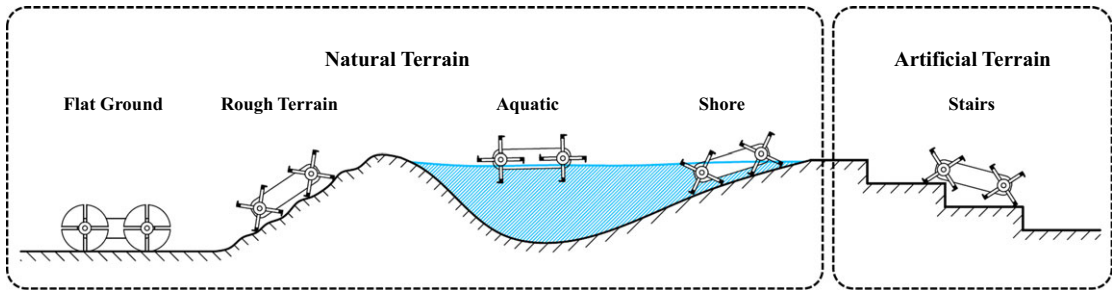


**Figure 1.** The locomotion strategies of WSP-bot in various terrestrial and aquatic environments.

1. A novel transformable wheel-spoke-paddle amphibious robot is designed, which achieves multi-modal cross-domain movement with small mass and compact size, providing an innovative and inspiring solution for small-scale amphibious robots.
2. Proposing a dynamic transformation method for mode switching during motion to effectively decrease transformation torque, thereby reducing workload and power consumption of actuators.
3. The proposed robot undergoes comprehensive theoretical analysis, simulations, and prototype testing to validate its multimodal cross-domain mobility.

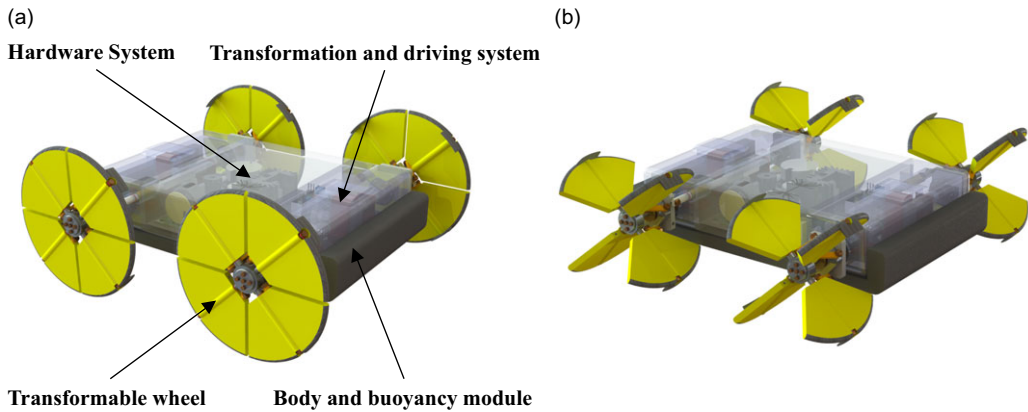
The remainder of this paper is organized as follows: Section 2 describes the mechanical design and control scheme of the robot. Section 3 presents the motion analysis of terrestrial transformation, movement, and obstacle-crossing. Section 4 conducts typical motion simulations on both land and water. Section 5 performs prototype testing for multimodal motion both indoors and outdoors. Finally, Section 6 concludes the paper.

## 2. Design of the wheel-spoke-paddle amphibious robot

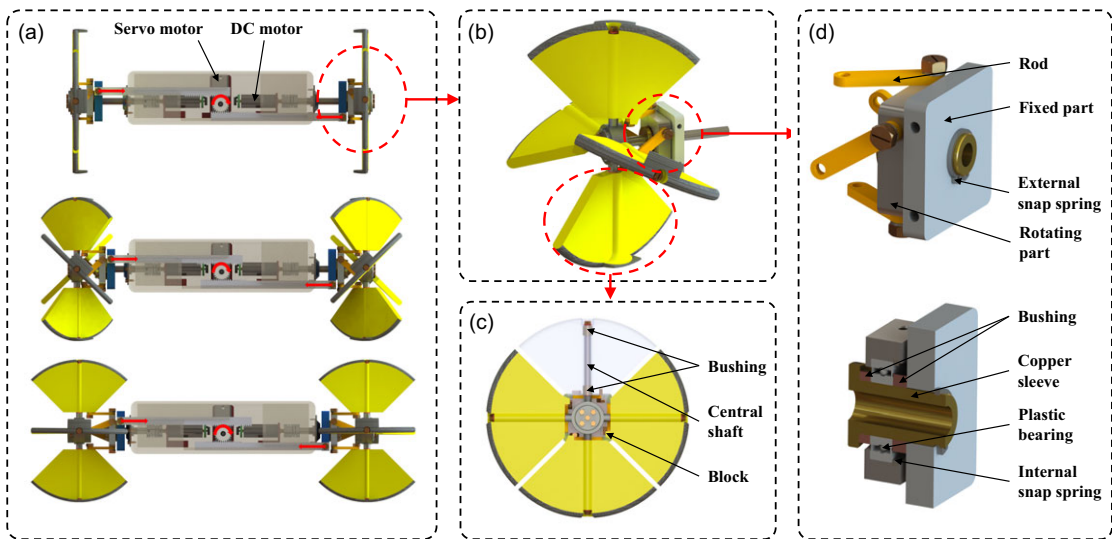
### 2.1. Overall design

Figure 1 illustrates the locomotion modes of the WSP-bot in various complex terrestrial and aquatic environments. The WSP-bot achieves multimodal cross-domain locomotion in natural and artificial environments through the transformation of its WSP module. For instance, the WSP-bot achieves rapid movement on flat terrain in wheel mode. When facing unstructured terrains such as grass, gravel, or uneven slopes, the robot switches to spoke mode to overcome these obstacles. When aquatic locomotion is required, the robot floats on the water surface, utilizing unfolded spokes as paddles to propel itself forward in a paddling manner. In addition, when operating in water-land transition zones such as shallow wetlands, the WSP-bot exhibits outstanding mobility compared to other amphibious robots due to the increased contact area with the ground provided by the transformable propulsion mechanism, which reduces the risk of sinking or wheel slippage. In the face of artificial terrain such as stairs, the robot can also overcome them effectively in spoke mode.

The WSP-bot is mainly composed of four sets of WSP modules, transformation and driving system, hardware system, a body, and a buoyancy module. Its wheel and spoke/paddle modes are illustrated in Fig. 2(a) and (b), respectively. Different from the radial expansion of most conventional transformable wheels [2, 5], the WSP module divides the complete wheel rim into four parts and directly folds the spokes radially by  $90^\circ$  to switch between wheel mode and spoke/paddle mode. The body of the WSP-bot primarily consists of the front and rear drive cabins and the central cabin, with the former containing the transformation and driving system and the latter accommodating the control hardware. The buoyancy module is located at the bottom of the body to provide buoyancy. It's noteworthy that the WSP-bot's spoke mode and paddle mode are essentially identical in configuration.



**Figure 2.** The 3D models of WSP-bot: (a) Wheel mode, (b) Spoke/Paddle mode.



**Figure 3.** Transformation and driving system: (a) Three different stages, (b) Single WSP module, (c) Detailed structure of spokes and hub inner ring, (d) Detailed structure of the axial push-pull unit.

The choice of transformation method has a significant impact on the mode switching of the robot. Most variable-shaped wheels use a dual-motor configuration with two parallel rotation axes, where one motor is responsible for transformation and the other for rotation [1]. However, this arrangement results in mutual interference between the transformation and rotation driving forces and is not conducive to reducing the number of actuators. The axial push-pull transformation scheme can effectively achieve the decoupling of transformation and rotation driving forces, while reducing the number of actuators. This approach has been successfully applied in the Passive Leg [31] and T-shape [32] configurations. Therefore, the WSP-bot employs an axial push-pull transformation method based on an offset crank-slider mechanism, where the slider serves as an active component to transmit axial forces along the axis for transformation, enhancing the reliability of transformation while simplifying the control approach.

The specific transformation and driving systems are illustrated in Fig. 3. Figure 3(a) sequentially shows the pre-transformation stage (wheel mode), the intermediate stage of transformation (propeller-like mode), and the post-transformation stage (spoke/paddle mode). The red rotating arrow represents

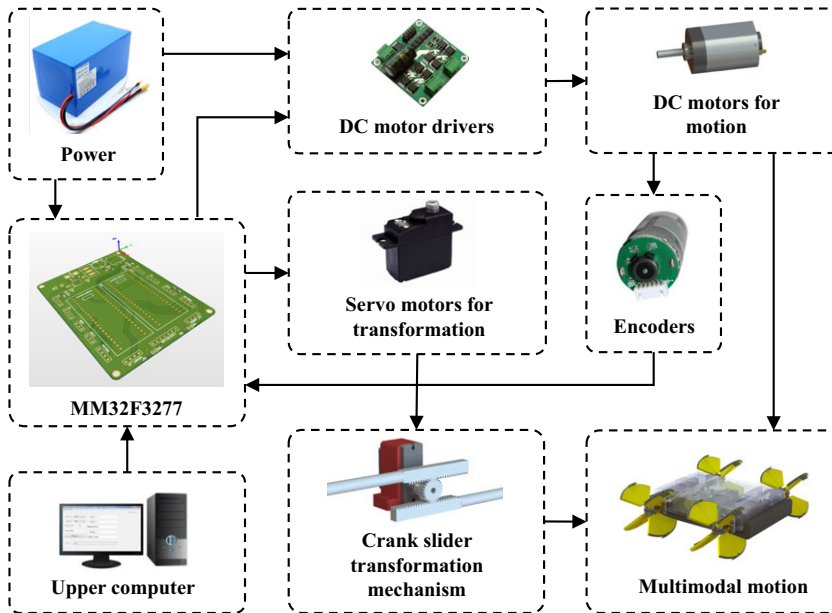


Figure 4. The control system of WSP-bot.

the transformation driving force generated by the servo motor, and the transmission of the transformation power is achieved through the gear-rack mechanism. The structure of the WSP module is presented in Fig. 3(b), which consists of 1/4 spokes and axial push-pull units connected by links. The connection between the spokes and the hub inner ring is shown in Fig. 3(c), where a single spoke is connected to the central shaft through two bushings to reduce friction. Each spoke has a block to limit the maximum transformation position. The structure of the axial push-pull unit is shown in Fig. 3(d), which mainly consists of fixed part, rotating part, connecting rods, copper sleeve, plastic bearing, etc. The far end of the rack is connected to the fixed part, driving the axial push-pull unit to slide along the axis and thus driving the offset crank-slider mechanism to realize the folding and unfolding of spokes. It should be noted that during the rotation of the WSP module, only the connecting rods and the rotating part are driven to move together, without affecting the fixed part. Therefore, the transformation and rotational motion are completely independent, rendering it feasible to switch the morphology at any moment during the locomotion process.

## 2.2. Control system design

The control system of the proposed robot is illustrated in Fig. 4. In this system, the upper computer sends motion commands to the MM32F3277 microcontroller, which receives and processes the instructions. Two PWM channels are utilized to directly control two servo motors, enabling the transformation of four WSP modules. Since the PWM signals from the microcontroller cannot drive the DC motors directly, communication between the microcontroller and the motor driver board is established. Eight PWM channels and full-bridge driver circuits are used to control the movement of WSP-bot by four DC motors. Four encoders measure the rotational speed signals of the DC motors, enabling the microcontroller to receive speed information and implement closed-loop control. Two rechargeable lithium batteries (7.4 V, 4000 mAh) are used to power the system, with step-down and step-up modules supplying power to the microcontroller, motor driver board, and other sensors.

**Table I.** Nomenclature.

Parameters	Definition
$R_s$	Radius of the WSP module in wheel mode
$\alpha$	Rotation angle of the WSP module during transformation
$\alpha'$	Angle between the connecting rod and the rotating part
$a$	Distance from the connecting point between the rod and the spoke to the central shaft
$b$	Length of the connecting rod
$e$	Offset distance of the equivalent slider
$d_g$	Pitch diameter of the gear
$m_w$	Mass of single WSP module
$m_b$	Mass of the body
$\delta$	Initial angle between the spoke and the ground when in spoke mode
$\beta$	Angle of the outer convex edge of the spokes
$\omega$	Angular velocity of the WSP module
$H$	Height of the obstacle
$P_1$	Front WSP module centroid position
$P_2$	Rear WSP module centroid position
$L$	Distance between $P_1$ and $P_2$
$X_{p1}$	Projection of the front spoke endpoint on the x-axis of the $P_1$ body coordinate system
$X_{p2}$	Projection of the rear spoke endpoint on the x-axis of the $P_2$ body coordinate system
$l_1$	Horizontal distance between the front spoke landing point and CoM of robot
$l_2$	Horizontal distance between the rear spoke landing point and CoM of robot
$F_{n1}$	Normal force of front spoke
$F_{n2}$	Normal force of rear spoke
$\theta$	Angle between body and horizontal plane
$\gamma$	Angle between the front spoke and the level of the obstacle when overcoming obstacles
$\epsilon$	Angle between the rear spoke and the ground when overcoming obstacles
$f$	Friction between the front spoke and the obstacle

### 3. Motion analysis

This section mainly discusses the kinematics and statics analysis of the transformation process and terrestrial locomotion. Table I lists the important parameters required for subsequent analysis of the WSP-bot. It is assumed that the robot is composed of rigid components, and there is no phase difference between the four WSP modules to simplify the analysis.

#### 3.1. Theoretical analysis of transformation torque

Initially, the variation of transformation torque was analyzed to select appropriate servo motors. As the initial positions differ, there are significant differences in the transformation torque when the robot switches from wheel-to-spoke mode. Therefore, in order to enable the robot to achieve mode switching in any state, the most demanding case in terms of transformation torque is selected for analysis, that is, when both spokes touch the ground in the initial state, as shown in Fig. 5(a).

A body coordinate system is established with the WSP module center as the origin  $o$ , as shown in Fig. 5(a). Each vector with the endpoint at the outer edge of the spoke is denoted as  $r_i$ , and the collection of these vectors is denoted as  $C_R$ , which is the orange area shown in Fig. 5(a). Thus:

$$r_i \in C_R = R_{\varphi,y}[R_s, 0, 0]^T \text{ where } \varphi \in [0, 45^\circ]. \quad (1)$$

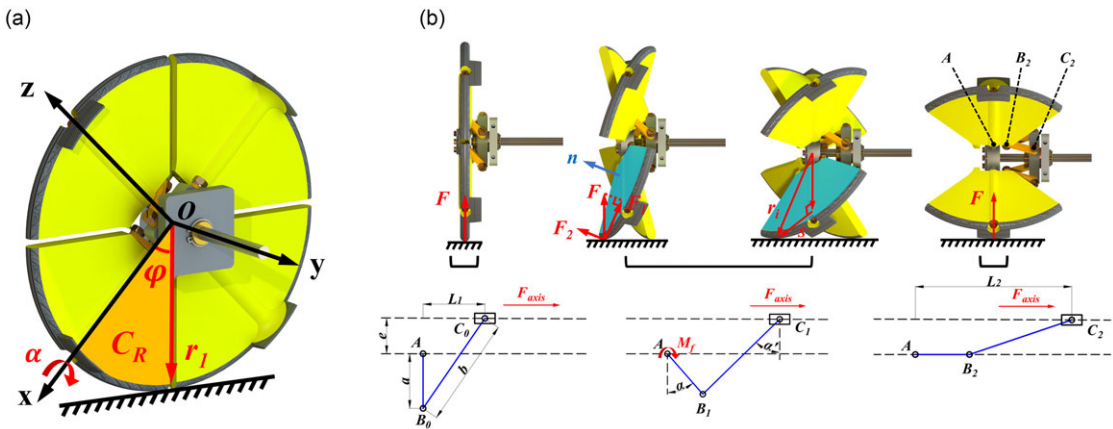


**Figure 5.** Analysis of the driving torque during transformation process: (a) Initial posture, (b) Decomposition of transformation and corresponding schematic of the crank-slider mechanism.

During transformation, the fixed vector  $r_1 = R_s[\sqrt{2}/2, 0, -\sqrt{2}/2]^T$  rotates along the  $x$ -axis of the body coordinate system and becomes  $r'_1$ , which can be expressed as:

$$r'_1 = R_{\alpha,x}r_1, \tag{2}$$

similarly:

$$r'_i = R_{\alpha,x}r_i, \tag{3}$$

where  $R_{\varphi,y}, R_{\alpha,x}$  are rotation matrices.

To simplify the analysis, the outer convex edge of the spoke is ignored, and the ground normal force is all equivalently applied to one of the spokes, while friction is neglected. The unit normal vector  $n$  perpendicular to the blue plane of the spoke in Fig. 5(b) can be obtained:

$$n = \frac{r'_i \times e_x}{|r'_i \times e_x|}, \tag{4}$$

where  $e_x$  is the unit vector along the  $x$ -axis. The projections of the normal force  $F$  onto the plane and its normal direction can be respectively obtained as  $F_1, F_2$ :

$$F_1 = (I_3 - nn^T)F, \tag{5}$$

$$F_2 = n^T F n, \tag{6}$$

where  $I_3$  is a  $3 \times 3$  identity matrix. Since  $F_1$  always intersects with the  $x$ -axis and exerts no torque on the spoke, it is only necessary to overcome the moment  $M_f$  generated by  $F_2$ :

$$M_f = |F_2|s, \tag{7}$$

where  $s$  is the distance from the normal force acting point to the central shaft, which is determined by  $r'_i$  when  $r'_i{}^T R_{45^\circ} e_x$  takes the maximum value:

$$s = |r'_i - e_x^T r'_i e_x|. \tag{8}$$

The relationship between the moment  $M_f$  and the driving force  $F_{axis}$  can be easily obtained:

$$M_f - F_{axis} \frac{a \sin(\alpha + \alpha')}{\sin \alpha'} = 0. \tag{9}$$

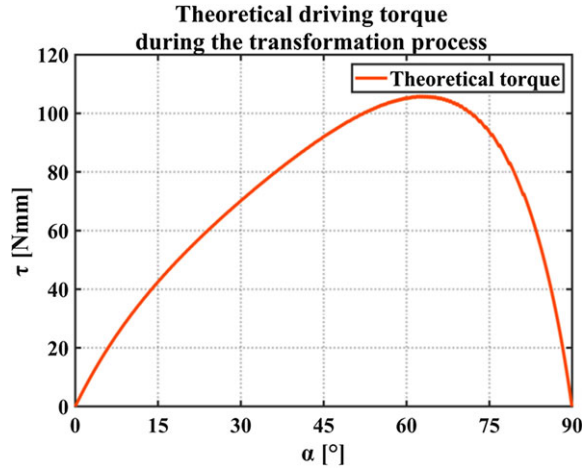


Figure 6. Theoretical transformation driving torque.

Additionally, there exists the following relationship between  $F_{axis}$  and driving torque  $M_d$ :

$$M_d = 2F_{axis}d_g. \tag{10}$$

Based on Eqs. (6)–(10), the driving torque  $M_d$  can be obtained as:

$$M_d = \frac{2 \sin \left( \arccos \left( \frac{a \cos \alpha + e}{b} \right) \right)}{a \sin \left( \alpha + \arccos \left( \frac{a \cos \alpha + e}{b} \right) \right)} |n^T F n| |r'_i - e_x^T r'_i e_x| d_g. \tag{11}$$

To analyze the variation of the driving torque, the parameters are set as follows:  $R_s=60$  mm,  $m_b=1$  kg,  $m_w=0.25$  kg,  $a=8$  mm,  $b=18$  mm,  $e=6.8$  mm,  $d_g=6$  mm. The theoretical driving torque during transformation is calculated and shown in Fig. 6. The overall driving torque shows a trend of increasing first and then decreasing, which is due to the fact that at the initial moment of transformation, the projection of the ground normal force  $F$  onto the blue plane is very small. As the spoke expands, the projection gradually increases, and the driving torque increases. When the folding angle is approximately  $65^\circ$ , the driving torque reaches a maximum of about 80 Nmm. Subsequently, the position of the ground normal force  $F$  quickly approached the central shaft, and  $s$  rapidly decreased, leading to a decrease in the driving torque. After the transformation is completed, the driving torque remained at zero due to the zero-lever arm of the normal force  $F$  with respect to the central shaft. It should be noted that although the analysis ignored the influence of the geometric shape of the protrusion at the end of the spoke, it has guiding significance for the selection of the transformation actuator.

### 3.2. Spoke mode on flat ground

When the robot moves on rough terrain, it transforms from wheel mode to spoke mode to achieve better mobility on land. Four different states of a single WSP module in spoke mode during flat terrain locomotion are shown in Fig. 7. The WSP module repeats four sets of movements within one revolution, with each set rotating by an angle of  $\pi/2$ . Within each set of movements, there are three processes: first, starting from the initial pose (Fig. 7(a)), the WSP module rotates along the outside of the spoke end protrusion (Fig. 7(b)); then, it rolls along the spoke end protrusion (Fig. 7(c)); finally, it rotates along



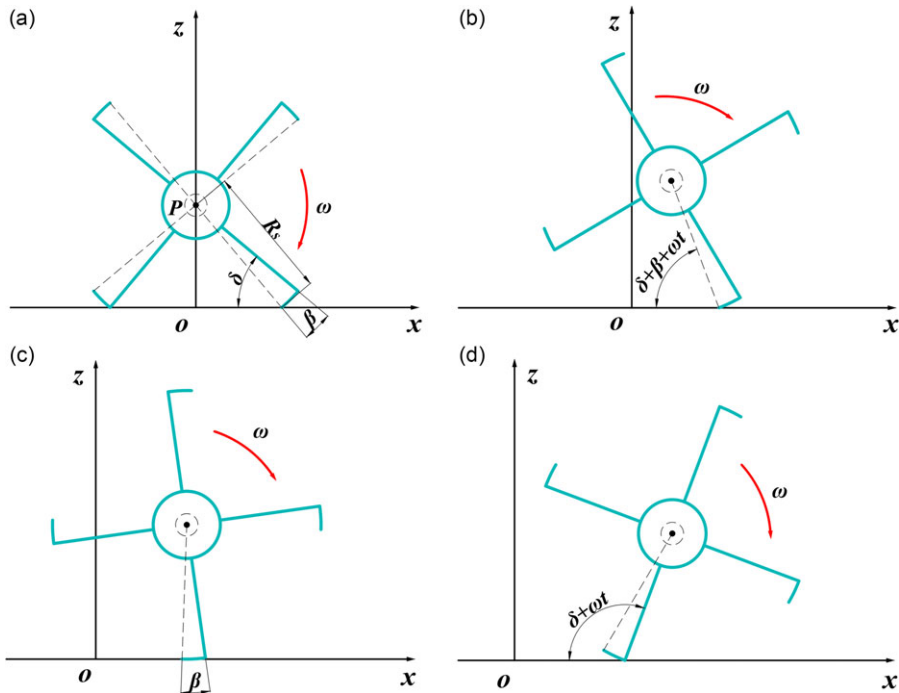


**Figure 7.** Different states of single WSP module in spoke mode on flat terrain: (a) Initial state, (b) Rotating along the outer edge, (c) Rolling along the edge, (d) Rotating along the inner edge.

the inside of the spoke end protrusion (Fig. 7(d)). The coordinate of the center movement for a single WSP module is as follows:

$$Z_p = \begin{cases} R_s \sin(\delta + \beta + \omega(t - kT)), & kT \leq t < \frac{\pi - 2\beta}{4\omega} + kT \\ R_s, \frac{\pi - 2\beta}{4\omega} + kT \leq t < \frac{\pi + 2\beta}{4\omega} + kT \\ R_s \sin(\delta + \omega(t - kT)), & \frac{\pi + 2\beta}{4\omega} + kT \leq t < \frac{\pi}{2\omega} + kT \end{cases}, \tag{12}$$

$$X_p = \begin{cases} R_s \cos(\delta + \beta) - R_s \cos(\delta + \beta + \omega(t - kT)), & kT \leq t < \frac{\pi - 2\beta}{4\omega} + kT \\ R_s \cos(\delta + \beta) + R_s(\beta - \frac{\pi}{2} + \delta + \omega(t - kT)), & \frac{\pi - 2\beta}{4\omega} + kT \leq t < \frac{\pi + 2\beta}{4\omega} + kT \\ R_s \cos(\delta + \beta) + R_s\beta + R_s \cos(\pi - \delta - \omega(t - kT)), & \frac{\pi + 2\beta}{4\omega} + kT \leq t < \frac{\pi}{2\omega} + kT \end{cases}, \tag{13}$$

where  $\delta = \pi/4 - \beta/2$ , cycle of single group motion  $T = \pi/2\omega$ , and  $k = 0, 1, 2, 3 \dots$ . Similarly, the velocity of the WSP module’s center can be obtained accordingly.

As the robot is driven by WSP modules both in the front and rear, the position of the robot’s CoM on the  $z$ -axis can be expressed as  $Z_{body} = (Z_{p1} + Z_{p2})/2$ . While using spoke mode can better overcome rough terrain, it also causes vibration and affects the stability of the robot.

### 3.3. Torque analysis for obstacle-crossing

When facing large obstacles that require the robot to overcome directly, the obstacle-crossing performance in spoke mode matters. Firstly, it is necessary to analyze the overall process of obstacle-crossing of the robot to select suitable driving motors. Figure 8 shows one of the stages of obstacle-crossing.

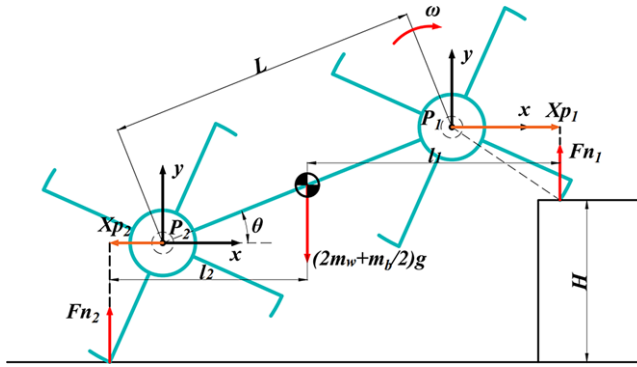


Figure 8. Illustration of WSP-bot in spoke mode during obstacle-crossing.

Body coordinate systems  $xP_1y$  and  $xP_2y$  are established at the centroid positions of the front and rear WSP modules, respectively. The following relationships can be obtained:

$$l_1 = \frac{L}{2} \cos \theta + X_{p1}, \tag{14}$$

$$l_2 = \frac{L}{2} \cos \theta - X_{p2}, \tag{15}$$

$$M_{d1} = \frac{l_2}{l_1 + l_2} mg X_{p1}, \tag{16}$$

$$M_{d2} = \frac{l_1}{l_1 + l_2} mg X_{p2}, \tag{17}$$

where  $M_{d1}$  and  $M_{d2}$  represent the torques of the front and rear motors, respectively. To evaluate the magnitude of the driving torque, the obstacle height  $H=60$  mm was chosen, and the obstacle-crossing process can be divided into eight stages, which can be obtained in Appendix.

The process of obstacle-crossing starts from the moment when the front spoke contacts with the obstacle and ends when the rear WSP module completely crosses over the obstacle. During this process,  $X_{p1}$ ,  $X_{p2}$ , and  $\theta$  all change, leading to changes in driving torque. The theoretical driving torques for the front and rear motors are shown in Fig. 9. In Figure 9(a), the yellow section represents the torque required for the front spoke to cross the obstacle, followed by the orange section where the front WSP module moves on flat terrain. The same applies to Fig. 9(b). The obstacle-crossing process ends at 4 rad. Therefore, for the WSP-bot with a total weight of 2 kg, at least 500 Nmm of driving torque is required to cross the obstacle smoothly.

### 3.4. The impact of obstacle height and angular velocity on obstacle-crossing

During obstacle-crossing, not only sufficient torque is required but also the endpoints of spokes maintain contact with the obstacle without sliding. The stable climbing process is determined by the normal force  $F_N$  and friction force  $f$ . As the theoretical driving torque of the front WSP module in Section 3.3 is significantly smaller than that of the rear one, the normal force on the front spoke is smaller than that on the rear spoke, making it more prone to slippage. Therefore, an analysis of the changes in the front normal force caused by parameter settings during obstacle-crossing is conducted to select an appropriate parameter range.

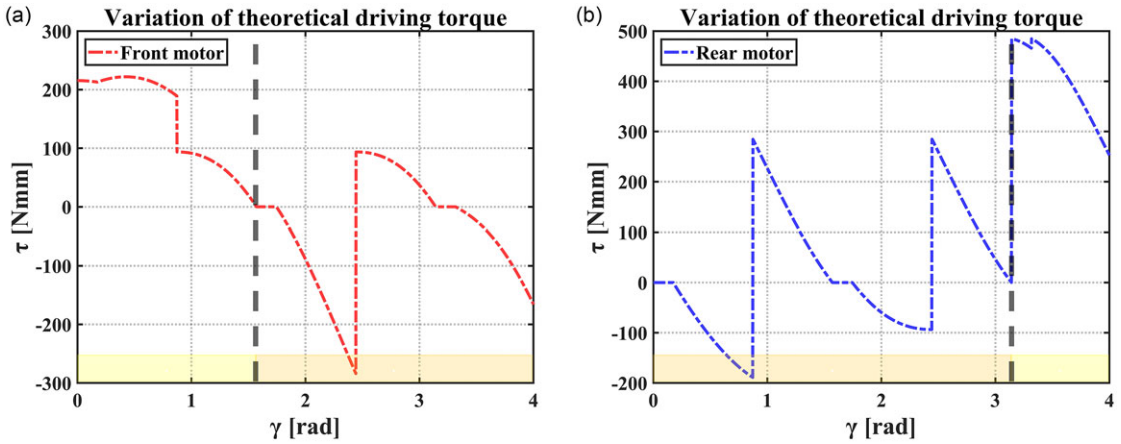


Figure 9. Theoretical driving torque during obstacle-crossing: (a) Front motor, (b) Rear motor.

The maximum height of obstacles that a single WSP module can theoretically overcome is:

$$H_{max} = 2R_s \sin\left(\frac{\pi}{4} - \frac{\beta}{2}\right) + R_s \left(\sin\left(\frac{\pi}{4} + \frac{\beta}{2}\right) - \sin\left(\frac{\pi}{4} - \frac{\beta}{2}\right)\right), \tag{18}$$

where  $H_{max}=84.5$  mm and  $\gamma \in [-2\pi/9, \pi/2]$ .

Figure 10(a)–(c) illustrates the front wheel obstacle-crossing process. During this process, the normal force  $F_{n1}$  and frictional force  $f$  are generated at point C. The static equilibrium equation is as follows:

$$\tau - M - F_{n1}R_s \cos \gamma - fR_s \sin \gamma = 0, \tag{19}$$

where  $\tau$  is the output torque of the front motor,  $M$  is the equivalent moment of the body acting on the CoM of front WSP module:

$$M = \frac{L}{4}m_b g \cos \theta. \tag{20}$$

By introducing the friction coefficient  $\mu = 0.3$  and substituting Eq. (19) and (20), the normal force  $F_{n1}$  can be obtained:

$$F_{n1} = \frac{\tau - \frac{L}{4}m_b g \cos \theta}{R_s (\cos \gamma + \mu \sin \gamma)}, \tag{21}$$

As shown in Fig. 10(a)–(c),  $\theta$  continuously increases and then remains constant. The two stages of  $\theta$  can be expressed as follows:

$$\theta = \begin{cases} \arcsin\left(\frac{H+R_s \sin \gamma - R_s \sin \epsilon}{L}\right), & \gamma < \frac{\pi}{4} - \frac{\beta}{2} \\ \arcsin\left(\frac{H}{L}\right), & \gamma \geq \frac{\pi}{4} - \frac{\beta}{2} \end{cases}. \tag{22}$$

The relationship between motor power, torque, and speed can be expressed as follows:

$$\tau = \frac{955P\pi}{3\omega}. \tag{23}$$

After starting the obstacle-crossing,  $F_{n1}$  acting on the front WSP module is as follows:

$$F_{n1} = \begin{cases} \frac{\frac{955P\pi}{3\omega} - \frac{L}{4}m_b g \sqrt{1 - \frac{(H+R_s \sin \gamma - R_s \sin(\frac{\pi}{2} - \gamma + \beta))^2}{L^2}}}{R_s(\cos \gamma + \mu \sin \gamma)}, & \gamma < \frac{\pi}{4} - \frac{\beta}{2} \\ \frac{\frac{955P\pi}{3\omega} - \frac{L}{4}m_b g \sqrt{1 - (\frac{H}{L})^2}}{R_s(\cos \gamma + \mu \sin \gamma)}, & \gamma \geq \frac{\pi}{4} - \frac{\beta}{2} \end{cases}. \tag{24}$$

To investigate the relationship between the front normal force  $F_{n1}$ , the speed  $\omega$ , and the obstacle height  $H$ , the motor power is set to  $P=2.46$  W. The obtained relationship between  $F_{n1}$  and  $H$  is shown in

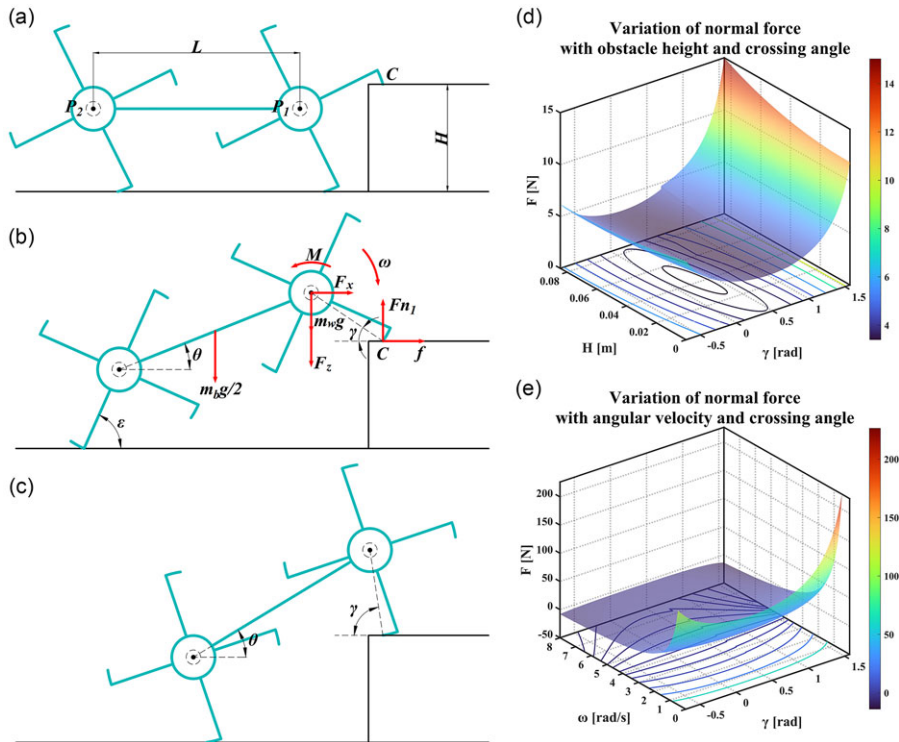


**Figure 10.** Front WSP module obstacle-crossing process and normal force  $F_{n1}$  analysis: (a) Initial posture, (b) Static analysis, (c) Obstacle-crossing about to be completed, (d) Relationship between  $F_{n1}$  and  $H$ , (e) Relationship between  $F_{n1}$  and  $\omega$ .

Fig. 10(d) at the condition of  $\omega=4$  rad/s. When  $\gamma$  increases,  $F_{n1}$  first decreases and then increases. This is because at the beginning of obstacle-crossing, the angle  $\theta$  between the body and the horizontal plane increases first and then remains constant. During the process of increasing  $\theta$ , the weight borne by the rear module increases as well. After  $\theta$  stops increasing, as  $\gamma$  gradually approaches  $\pi/2$ , the CoM of the body is closer to the front contact point. Similarly, Fig. 10(e) shows the effect of the speed  $\omega$  on  $F_{n1}$ . Because the motor power is assumed to be constant, there is an inverse proportionality between the motor speed and torque. As the speed  $\omega$  increases,  $F_{n1}$  gradually decreases. When  $\omega>3$  rad/s,  $F_{n1}$  decreases rapidly, and the negative values in the figure indicate that there is a high risk of slipping. When  $\omega<0.5$  rad/s, the force value is very large but not stable. When  $1.5$  rad/s  $< \omega < 2.5$  rad/s, the force value is relatively suitable and stable.

## 4. Simulation experiment

### 4.1. Simulation of wheel-spoke transformation and recovery

To verify the effectiveness of the transformation mechanism, virtual prototype simulations are conducted using Adams. First, simulations of transformation and recovery are performed under different initial states on flat ground. The initial state when both spokes of the WSP module touch the ground is set to  $0^\circ$ , and states at  $15^\circ$ ,  $30^\circ$ , and  $45^\circ$  are shown in Fig. 11.

The transformation and recovery driving forces provided by servo motors are shown in Fig. 12(a) and (b), respectively. The required servo torques for transformation and recovery vary greatly with different initial states, but their trends are similar. Taking the initial state of  $0^\circ$  as an example, the entire transformation process lasts for 10 s:

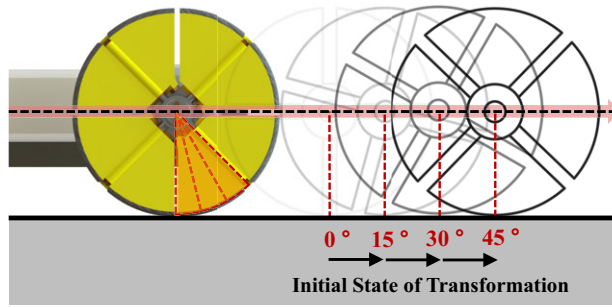


Figure 11. Initial state selection for mode transformation: 0°, 15°, 30°, 45°.

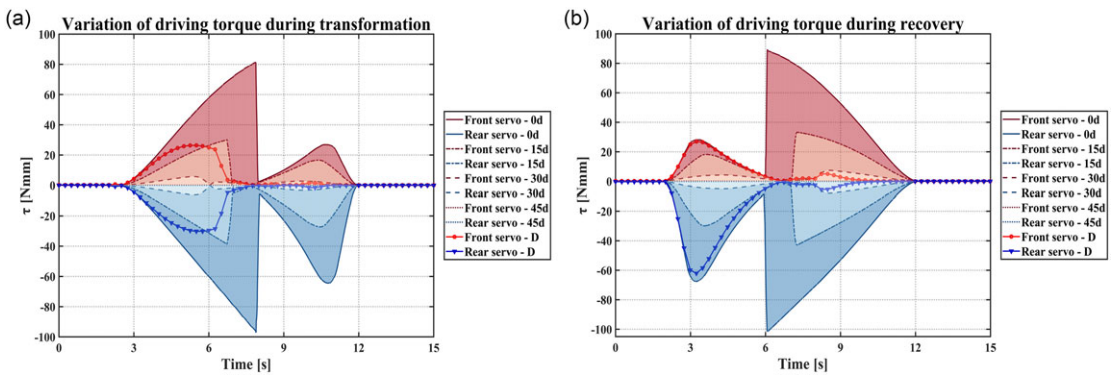


Figure 12. Variation of servo torque during transformation and recovery: (a) Torques under different initial states during transformation, (b) Torques under different initial states during recovery.

- (1) Starting at 2 s, the transition occurs, accompanied by an increase in driving force from zero;
- (2) At approximately 8 s, the driving force decreases significantly, which can be attributed to the structural characteristics of the protruding part on the outer edge of the spokes, resulting in discontinuous changes in the contact point between the spoke and the ground;
- (3) Subsequently, the side of the protruding part on the outer edge of the spoke maintains contact with the ground and continues to transform, and the driving torque continues to increase.
- (4) At around 11 s, the contact point changes from the side to the front, and the transformation is basically completed.

The transformation and recovery process with an initial state of 0° is shown in Fig. 13(a) and (b). Since the robot needs to be lifted during the recovery process to overcome gravity, the servo torque is greater than that during the transformation process, and the torque changes in the opposite direction. Due to the structural characteristics of the spoke itself, the torque changes at the initial states of 15° and 30° compared to 0°. When the initial state is 45°, the required torque is minimal since only friction needs to be overcome during the mode switching.

#### 4.2. Dynamic transformation method

According to the analysis in Section 4.1 and the variation shown in Fig. 12(a) and (b), the initial state of the spoke has a significant impact on the required servo torque. As the initial angular state progressively increases from 0° to 45°, there is a marked reduction in both transformation and recovery torque. Nonetheless, achieving accurate control of the initial angular state proves to be difficult in practical applications. For instance, when transitioning from spoke mode to wheel mode, in the absence of PWM

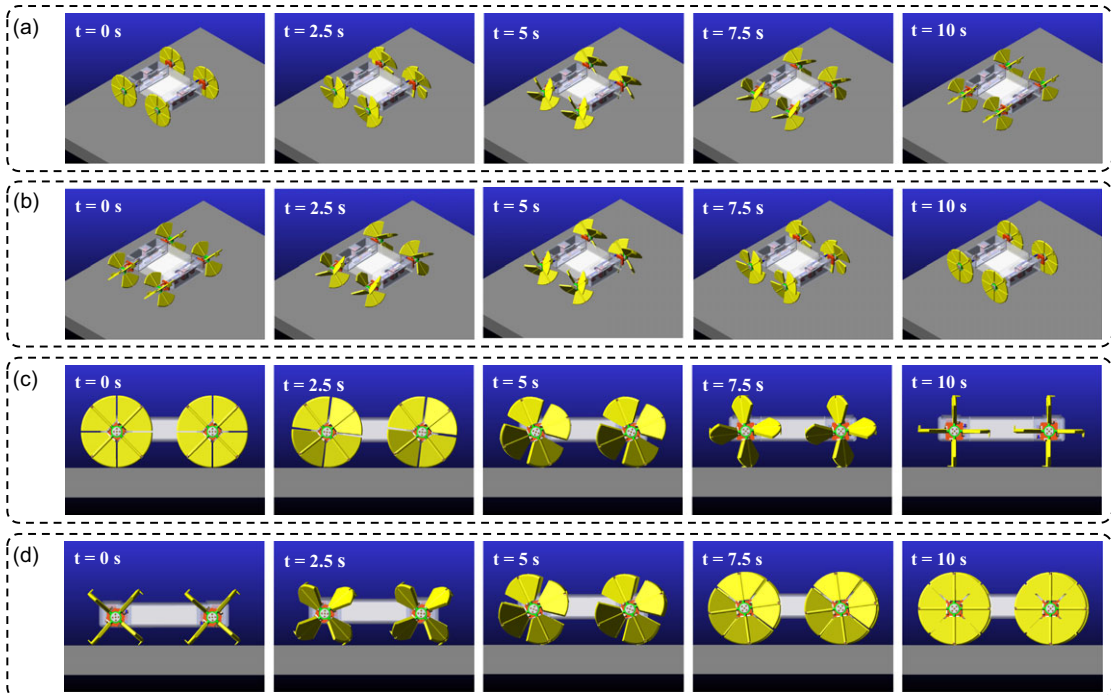


**Figure 13.** Mode transformation simulation: (a) Transformation from initial state of  $0^\circ$ , (b) Recovery from initial state of  $0^\circ$ , (c) Transformation with dynamic method, (d) Recovery with dynamic method.

motor control signals, gravity causes two spokes in each WSP of the robot to make simultaneous contact with the ground, typically resulting in an initial state of  $0^\circ$ . Consequently, a dynamic transformation method is proposed that effectively reduces the torque on the front and rear servo motors.

As depicted in Fig. 12(b) by the red circular dashed line representing Front servo-D and the blue triangular dashed line representing Rear servo-D, the motors rotate at a constant speed while the servos are operating, and during this recovery process, the WSP gradually rotates from the initial position of  $0^\circ$  to  $45^\circ$ . The servo torque exhibits an initial increase followed by a decrease, subsequently stabilizing within a relatively minor torque range of  $\pm 30$  Nmm, thus precluding further escalation in servo torque. This strategy can similarly be applied to reduce driving torque during the transformation from wheel-to-spoke mode, as demonstrated by Front servo-D and Rear servo-D in Fig. 12(a). Figure 13(c) and (d) separately display the wheel-to-spoke and spoke-to-wheel processes employing this method. Utilizing this transformation approach can effectively protect the servos, reduce the workload, and lower energy consumption.

### 4.3. Obstacle-crossing

To validate the obstacle-crossing performance, an obstacle-crossing simulation is conducted, as depicted in Fig. 14. The robot initially moves on a horizontal surface in wheel mode and subsequently undergoes transformation to spoke mode to surmount higher obstacles. Upon clearing the obstacle, it reverts back to its wheel configuration.

Within the simulation, the obstacle height is set to 60 mm, and the angular velocity of WSP module is set to 1.5 rad/s. The torques of the front and rear motors in spoke mode are illustrated in Fig. 15. The orange segment in the figure signifies the spoke mode on a level terrain, and the yellow segment represents the process of overcoming the obstacle. The robot commences the obstacle-crossing approximately 1.1 s subsequent to the transformation from wheel-to-spoke mode.

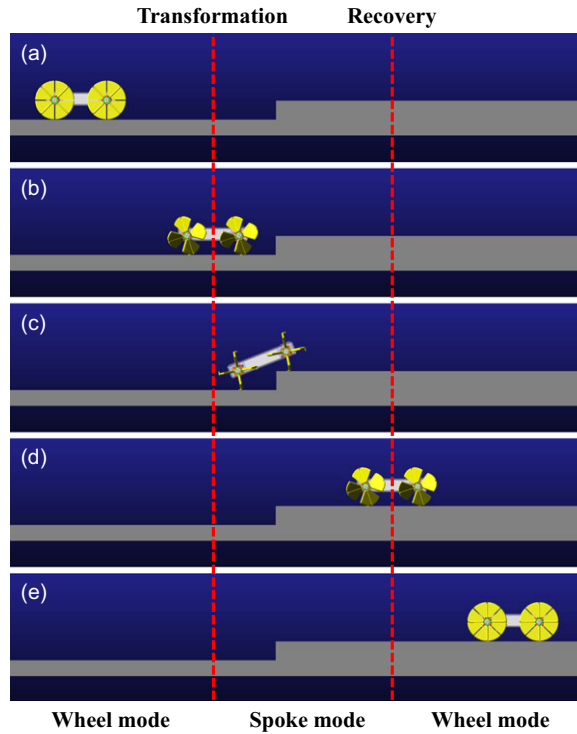


**Figure 14.** Obstacle-crossing simulation: (a) Wheel mode, (b) Transformation, (c) Obstacle-crossing process, (d) Recovery, (e) Wheel mode.

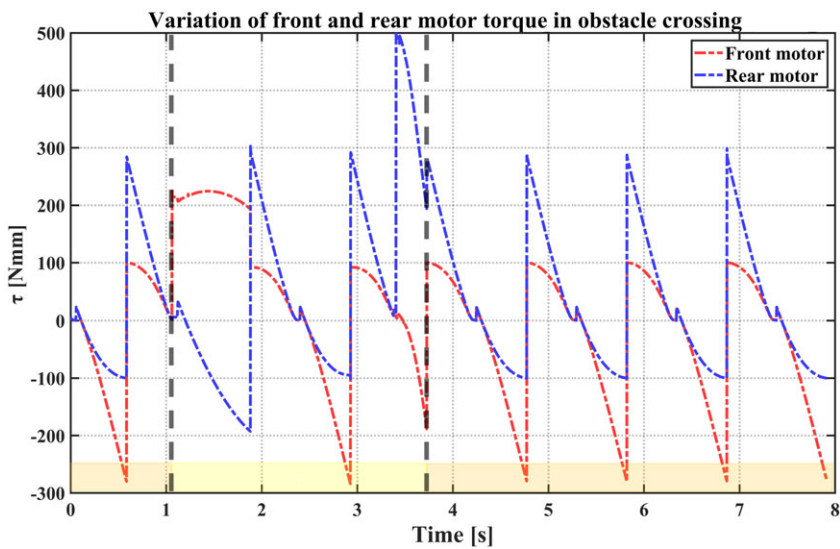


**Figure 15.** Variations of front and rear motor torques in spoke mode during obstacle-crossing.

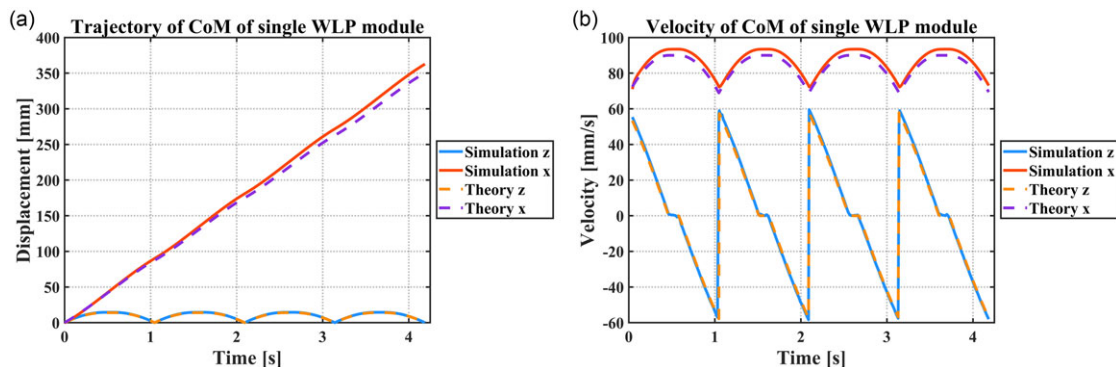


**Figure 16.** The CoM of WSP module on flat ground in spoke mode: (a) Displacement of simulation and theoretical analysis, (b) Velocity of simulation and theoretical analysis.

Throughout the obstacle-crossing process, the maximum torque exerted by the rear motor is approximately 500 Nmm, surpassing the maximum torque of 300 Nmm of the front motor. The change in trend is generally congruent with the theoretical torque presented in Section 3.3. The obstacle-crossing concludes at approximately 3.7 s, with the robot subsequently moving on flat terrain in spoke mode, while the CoM of the robot undergoes periodic oscillations.

Subsequent to the completion of the obstacle-cross and during the spoke motion on level terrain, the position and velocity of the CoM for an individual WSP module are demonstrated in Fig. 16, exhibiting a high degree of consistency with the theoretical trajectories. Concurrently, the robot's maximum obstacle-crossing height in wheel mode, as well as its success rate in traversing obstacles of varying heights in spoke mode were evaluated. The results demonstrate that in wheel mode, the WSP-bot can successfully surmount obstacles with a maximum height of approximately 22 mm at a rotational speed of 1.5 rad/s. In spoke mode, it exhibits the capability to stably traverse obstacles below 65 mm in height at any attainable angular velocity within its operational range.

#### 4.4. Aquatic thrust simulation

A simulation of aquatic thrust for a single WSP module was conducted using Fluent to verify whether the WSP module can generate sufficient propulsion force on the water surface. The specific parameters of the simplified model and simulation environment are shown in Table II. The unstructured mesh is employed for grid division. The inlet boundary condition is set to velocity-inlet with 0.1 m/s, while the outlet boundary condition is designated as an out-flow type. The VOF model and  $k - \epsilon$  turbulence model are employed to address the water-air interface and turbulence issues. The detailed simulation environment is illustrated in Fig. 17.

In the computational initialization, the rotational angular velocity of the WSP module is set to 240 rpm. The simulation time step is set to 0.0001 s, with a total of 5000 steps, simulating the continuous rotation for 0.5 s from a stationary state. The resulting three-dimensional flow field phase diagrams are shown in Fig. 18, displaying the flow field states at four distinct time instances.

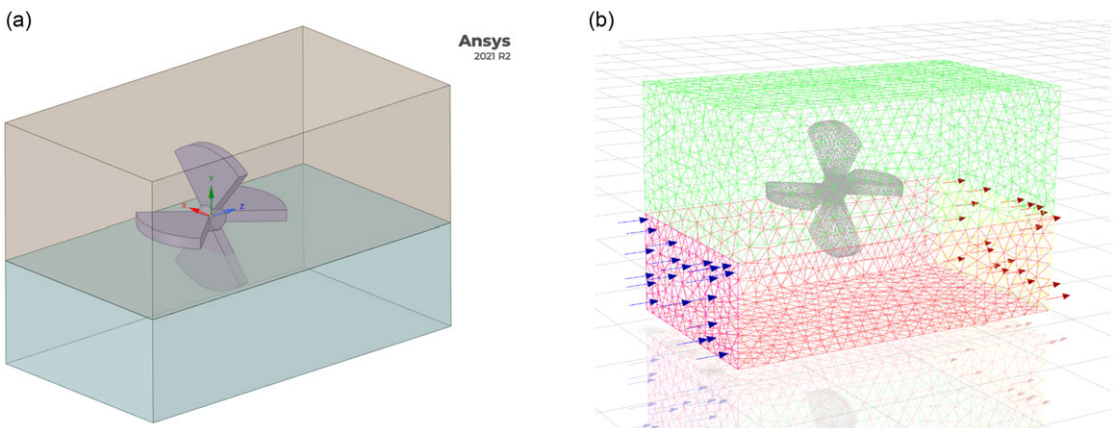
Figure 19(a) records the variations in force along the  $z$ -axis during the 0.5 s rotation process. As the WSP module starts rotating from a standstill and the water surface remains calm, the thrust is relatively large and varies dramatically. After 0.3 s, when the paddles have fully agitated the water flow, the thrust stabilizes and the average thrust generated in the  $z$ -axis direction is approximately 0.391 N.

Moreover, to model the maximum drag force, the fuselage is fully submerged in water, with the water flow velocity set at 0.1 m/s. As illustrated in Fig. 19(b), it encounters a drag force of approximately 0.037 N, which indicates that the WSP module can provide sufficient thrust to enable movement on the water surface.



**Table II.** Specific parameters of single WSP module and simulation environment.

Parameters of simplified model or simulation environment	Value
Diameter of the spoke $D$	120 mm
Maximum width of the spoke $W$	72 mm
Thickness of the spoke $T$	8 mm
Number of spokes $N$	4
Spoke depth into water $H$	30 mm
Distance from the water inlet to the center of the paddle	$1.2D$
Distance from the water outlet to the center of the paddle	$1.8D$
Width of water/air domain	$1.5D$
Height of the upper air domain	$1.5D$
Height of the lower water domain	$1D$

**Figure 17.** Fluent simulation environment: (a) Simplified model, (b) Inlet/Outlet configuration and mesh partitioning.

## 5. Experimental results and discussion

Based on the analysis and simulation presented above, the prototype of the robot designed in this paper is shown in Fig. 20. Figure 20(a) illustrates the wheel mode, while Fig. 20(b) shows the spoke/paddle mode. The basic parameters of the robot are listed in Table III.

To achieve speed control of the robot, closed-loop control is implemented through encoders in all four WSP modules. The speed of the motors on the left and right sides of the robot will track the target speed, enabling overall speed control and left/right turning. The host computer can set the target speed and switch modes wirelessly during the robot's movement.

### 5.1. Flat ground locomotion

Initially, experiments on terrestrial wheeled locomotion were conducted. Figure 21 displays the process of the WSP-bot's wheeled locomotion and obstacle avoidance on land. The robot moved smoothly on land with wheels. When faced with an insurmountable obstacle, the robot completed a left turn within 4 s, with a turning radius of approximately twice its body length. It then made a right turn to resume its original direction and continued moving forward with wheels. The speed curve during the process is shown in Fig. 22(a). It is worth noting that the motor angular velocity values were obtained by reading the number of pulses per unit time through encoders and then converting the values. Owing to ground friction, the closed-loop control effect needs to be improved, but the robot was able to accomplish speed

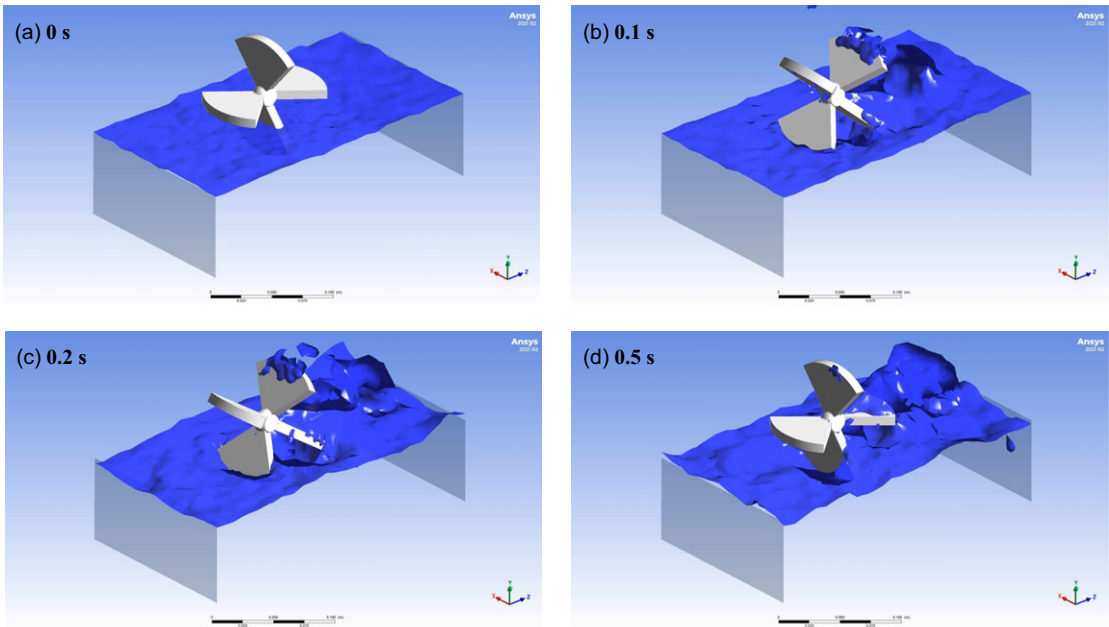


**Figure 18.** Three-dimensional flow field variation diagrams: (a) Initial state, (b) Start of rotation, (c) Near completion of one revolution, (d) Completion of two revolutions.

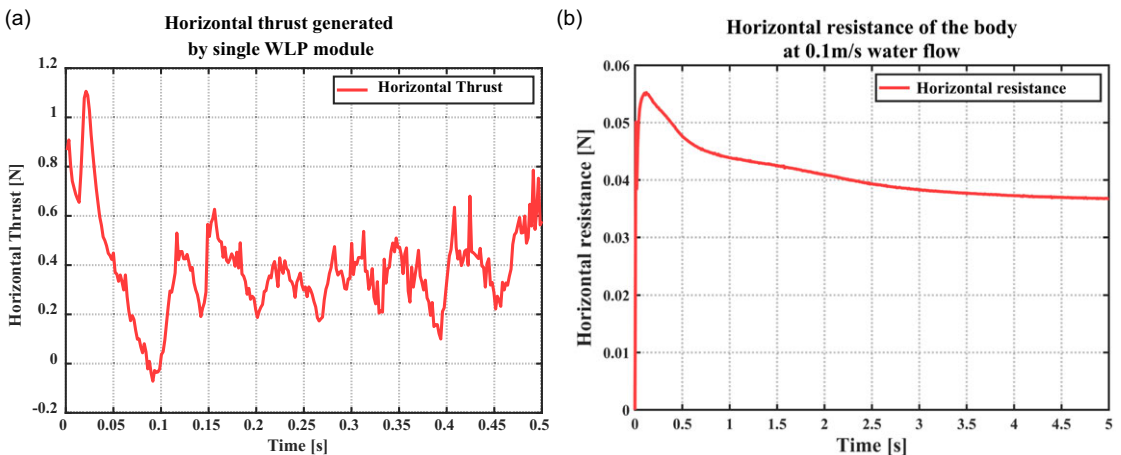


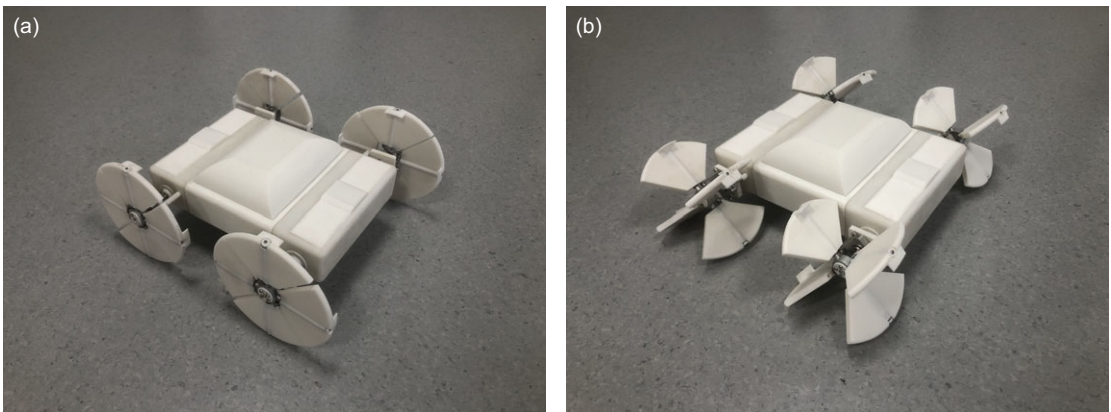
**Figure 19.** Horizontal thrust/resistance variation: (a) Horizontal thrust generated by single WSP module, (b) Resistance experienced by the fuselage.

tracking and left/right turning. Furthermore, the maximum speed of the WSP-bot in wheel mode on land is approximately 0.8 m/s. This obstacle avoidance method enables the robot to circumvent large obstacles on land without having to surmount them directly.

Additionally, a comparison of the speed and stability on flat terrain was conducted between the wheel and spoke modes, as illustrated in Fig. 23. Both modes had a motor angular velocity of 3 rad/s and a movement duration of 20 s, shown in the supplementary video. Since the spoke mode's WSP modules essentially act as rotating legs and benefit from closed-loop control, the speeds in both modes are comparable. The spoke mode speed is slightly higher, primarily because of the smooth ground and the robot's inertia, causing it to slide forward upon contact with the ground. However, as evidenced by the

**Table III.** Robot parameters.

Parameters of overall size and WSP module	Value
Overall dimension in wheel mode	280×239×120 mm
Overall dimension in spoke/paddle mode	280×316×120 mm
Weight	1.34 kg
Spoke length	46 mm
Spoke end outer protrusion angle	10°
Spoke thickness	6 mm
Rod length	18.5 mm
Diameter in wheel mode	120 mm

**Figure 20.** Prototype of the robot: (a) Wheel mode, (b) Spoke/Paddle mode.

trajectory of CoM in Fig. 23, the wheel mode can achieve higher speeds while maintaining excellent stability and smoothness. In contrast, the impact generated by excessive speed in spoke mode could be catastrophic, limiting its maximum speed.

## 5.2. Obstacle-crossing

In the obstacle-crossing experiment, the robot attempted to overcome obstacle of the same 60 mm height at an angular velocity of 3 rad/s in both wheel mode and spoke mode. Figure 24 illustrates the complete obstacle-crossing process in both modes, as also shown in the supplementary video.

In wheel mode, the robot maintained a constant forward velocity, preserving its original configuration, and made direct wheel contact with the obstacle. However, the wheels continuously rotated, resulting in slippage and the robot was unable to overcome the obstacle. The entire process is depicted in Fig. 24(a).

The complete obstacle-crossing process in spoke mode, presented in Fig. 24(b), including wheeled movement, transformation, spoke mode obstacle-crossing, and recovery, was performed within 30 s as follows:

- (1) 0–6 s: The robot moved rapidly on land with wheels. Nonetheless, it was unable to surmount the obstacle in wheel mode.
- (2) 6–10 s: The robot stopped in front of the obstacle and switched from wheel-to-spoke mode using the dynamic transformation method.
- (3) 10–18 s: The robot successfully crossed the obstacle in spoke mode, and proceeded to move a short distance on flat ground.

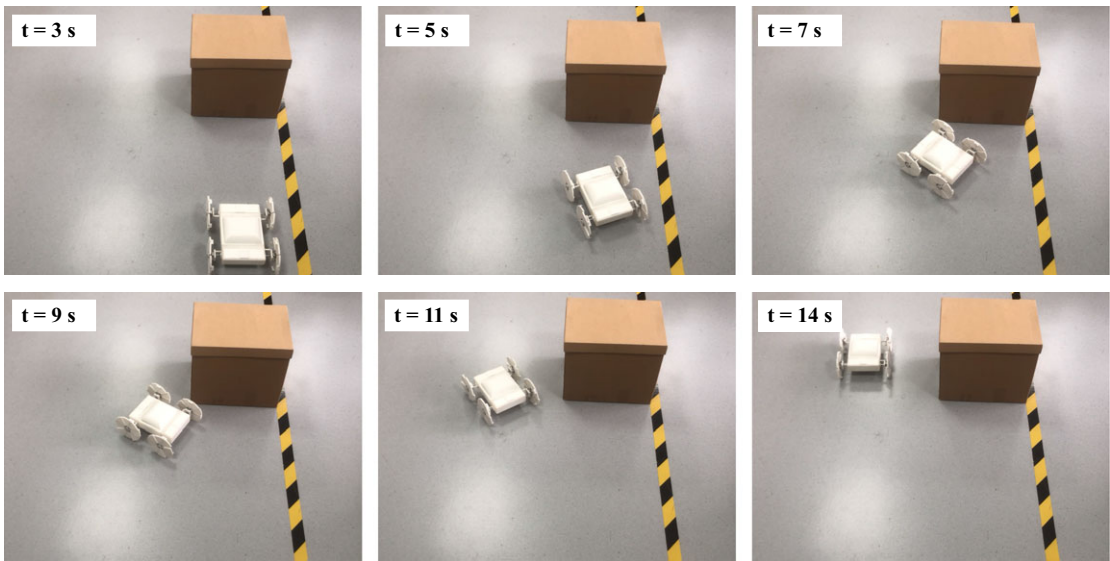


**Figure 21.** Terrestrial wheeled locomotion and obstacle avoidance.

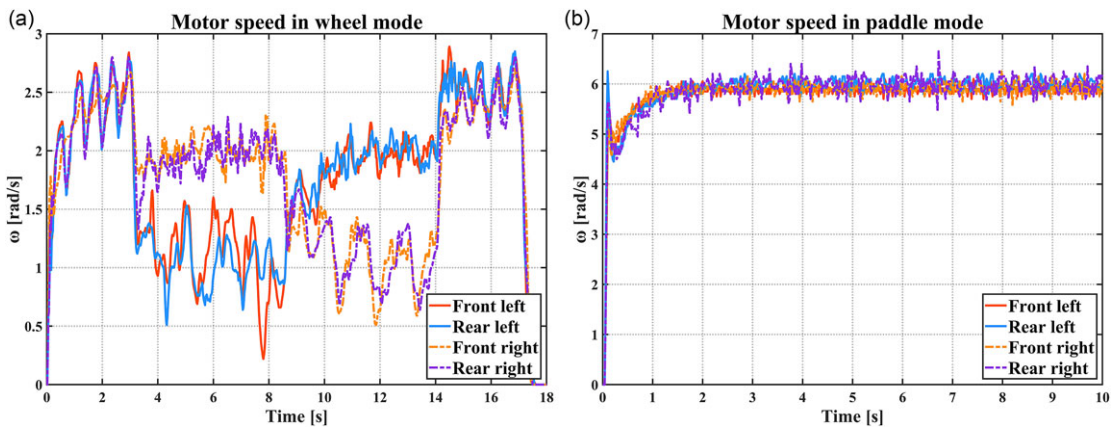


**Figure 22.** Motor speed: (a) Wheel mode on land, (b) Paddle mode on water.

(4) 18–22 s: After completely crossing the obstacle, the robot employed the dynamic transformation approach to revert from spoke mode to wheel mode.

(5) 22–24 s: The robot resumed its swift movement on flat ground in wheel mode.

During the process of crossing obstacles, the robot's rear legs require a significant amount of torque to climb over the obstacles. To achieve successful obstacle-crossing, closed-loop control is implemented to enable the motors to output sufficient torque. To explore the effect of motor angular velocity  $\omega$  and obstacle height  $H$  on the success rate of obstacle-crossing, experiments were performed with various angular velocities and obstacle heights in spoke mode. Each parameter combination was tested five times, and the results are presented in Table IV. It can be inferred that the robot can stably cross obstacles up to 65 mm in height, with an obstacle-crossing ratio of 1.08 (ratio of the maximum obstacle height to the transformed spoke length). Furthermore, the robot demonstrates stable obstacle-crossing capability at an angular velocity of approximately 2 rad/s.

When the angular velocity surpasses 2.5 rad/s, the robot's body exhibits severe oscillations, with the possibility of the rear legs being able to surmount higher obstacles. However, it is imperative to acknowledge that the obstacle-crossing process at excessively high angular velocities is unstable, leading

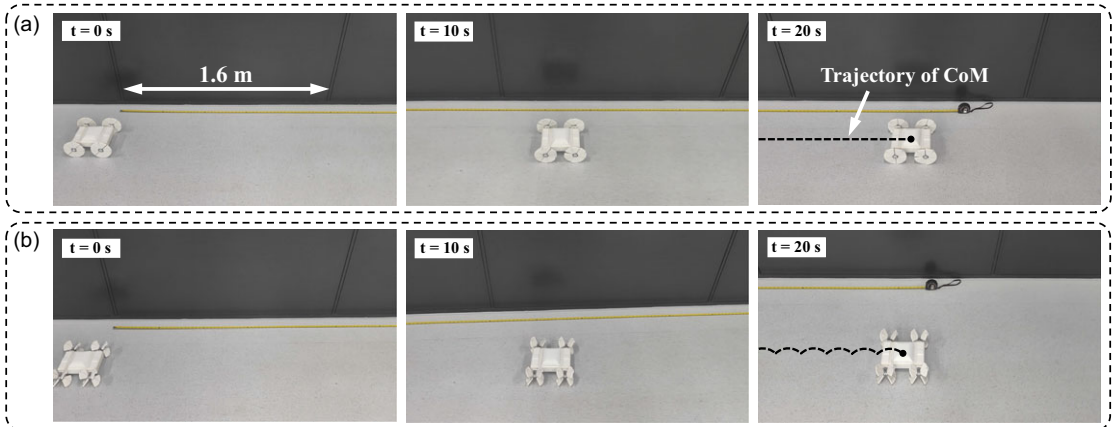


**Figure 23.** Comparison of speed and smoothness on flat terrain between wheel and spoke modes: (a) Wheel mode, (b) Spoke mode.

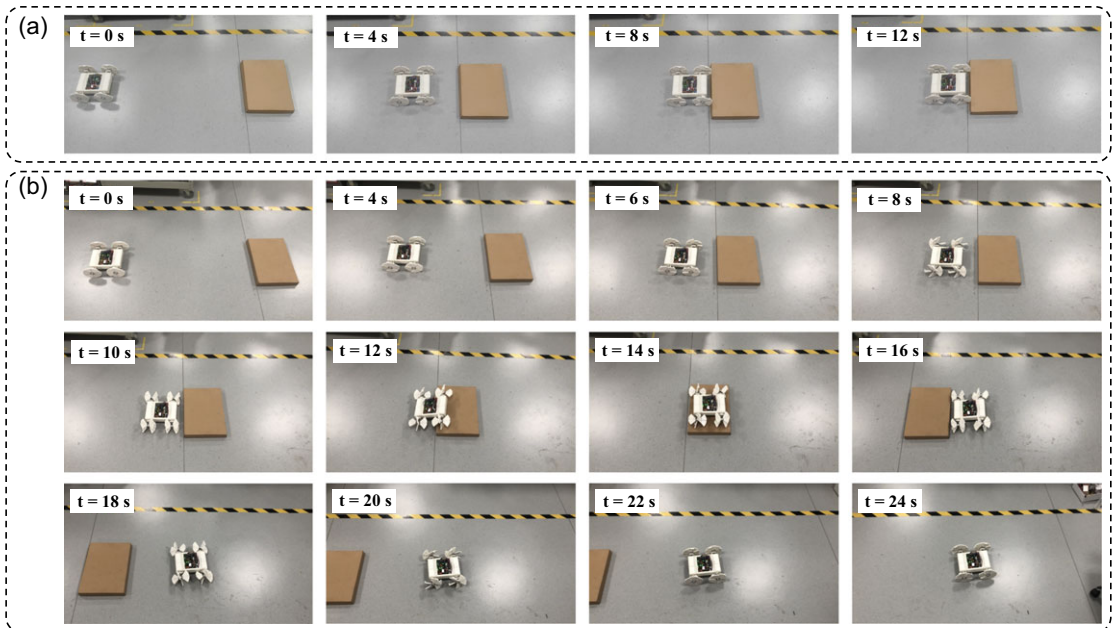


**Figure 24.** Comparison of obstacle-crossing performance in wheel mode and spoke mode: (a) Unable to overcome obstacle in wheel mode, (b) Transformation, successful obstacle-crossing in spoke mode and recovery.

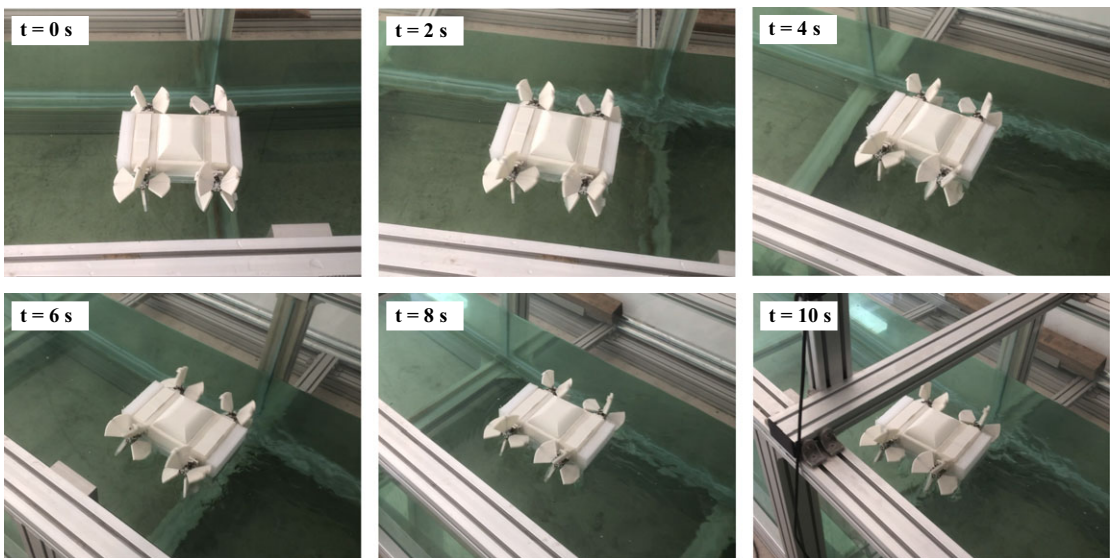
to detrimental impacts on the robot. Therefore, employing angular velocities exceeding 2.5 rad/s for obstacle-crossing is deemed inadvisable.

### 5.3. Aquatic locomotion

The aquatic locomotion capability of WSP-bot was verified through water surface propulsion experiment conducted in a narrow pool. The additional 2 cm float added to the bottom of the robot provides sufficient buoyancy on water. The target rotational speed for all motors is set to 6 rad/s, as illustrated in Fig. 25, illustrating the motion initiated from a state of rest.

**Table IV.** Success rate at different heights and angular velocities in spoke mode.

$H$ (mm)	$\omega$ (rad/s)						
	1	1.5	2	2.5	3	3.5	4
50	100%						
55							
60							
65							
70	0%			<50%		>50%	
75				<50%		>50%	
80	<50%						
85							

**Figure 25.** Aquatic locomotion in paddle mode.

The robot underwent an acceleration phase from 0-2 s and then gradually stabilized, achieving an average speed of approximately 0.2 m/s over the entire process. The motor speeds are illustrated in Fig. 22(b). Due to reduced resistance, the closed-loop control of the motors during water surface motion is more effective than land-based wheeled mobility, achieving the set rotational speed within 1.5 s after the initiation of motion with no overshoot. When the motors operate at full duty cycle, the maximum achievable water surface movement speed is approximately 0.26 m/s. Furthermore, o-ring seals and waterproof end caps are used for dynamic sealing at the connection point between the shaft and the front and rear drive cabins. Sealant is applied at the junctions between the front and rear drive cabins and the central cabin for waterproofing.

#### 5.4. Outdoor/Field experiments

Outdoor/Field trials evaluated the mobility of WSP-bot in various outdoor environments, as depicted in Fig. 26. Figure 26(a) demonstrates rapid and smooth wheel mode movement, while Fig. 26(b) tests the robot's ability to transform and recover on outdoor terrain. The robot could achieve mode transitions on

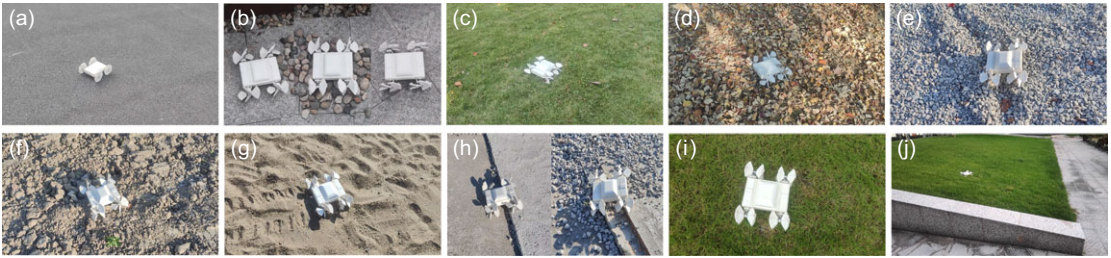


**Figure 26.** Outdoor/Field experiments: (a) Rapid wheel movement, (b) Transformation and recovery, (c) Grassland, (d) Leaf-covered terrain, (e) Gravel ground, (f) Unstructured terrain, (g) Sand, (h) Obstacle-crossing, (i) Muddy terrain after rain, (j) A 10° slope with tall grass.

almost all flat surfaces. Similarly, spoke mode performance was verified in complex outdoor environments such as grassland, leaf-covered terrain, gravel ground, unstructured terrain, and sand, as shown in Fig. 26(c)–(g), exhibiting excellent performance.

Notably, the mobility of the wheel mode was also tested on unstructured and sandy terrains. Due to its limited obstacle-crossing capability and susceptibility to getting stuck in soft terrains like sandy roads, wheel mode had limitations. In contrast, spoke mode performed well. Additionally, WSP-bot in spoke mode successfully climbed steps (Fig. 26(h)), adapted to muddy terrain after rain (Fig. 26(i)), and ascended a 10° slope with tall grass (Fig. 26(j)). Further details are available in the supplementary video.

### 5.5. Analysis and prospects

Based on the aforementioned experiments, WSP-bot has effectively executed terrestrial wheeled movement, mode transition, and recovery, obstacle-crossing in spoke mode, water surface locomotion, and outdoor/field experiments. Although WSP-bot effectively balances flat terrain mobility stability, obstacle traversal capability, and water surface movement ability, it also introduces some performance tradeoffs. Firstly, the WSP module may struggle to keep a constant  $\alpha$  angle precisely due to ground friction in wheel mode, meaning it has difficulty in maintaining the standard wheel configuration accurately. Additionally, thin spokes and incomplete rims result in a lower effective payload capacity for the robot. The current weight of the robot, without the addition of any external sensors, is 1.34 kg. Through testing, its maximum payload capacity is approximately 1 kg (0.8 times its own weight). When exceeding this weight limit, it becomes more challenging to maintain the angle of the WSP module during steering in wheel mode, and mode transitions may not occur smoothly. Given that the initial design intent of WSP-bot was for it to be small and lightweight, this issue is considered tolerable, but it warrants further improvement.

While the robot can achieve a speed of approximately 1 bodylengths/s on water, it is undeniable that the thickness of the float will have an impact on its ability to overcome obstacles on land. Balancing both aspects is also a crucial issue and worth further optimization in the future. During field experiments, the robot sometimes struggles to switch modes on non-flat terrain due to branches or stones getting stuck between spokes. Therefore, mode transition on flat ground is more recommended.

The comparative results between WSP-bot and some previously published amphibious robots or similarly sized terrestrial mobile robots are shown in Table V. It can be observed that WSP-bot balances multimodal cross-domain mobility capabilities, encompassing smooth wheeled motion, obstacle traversal, and aquatic movement. While some amphibious robots exhibit higher speeds, they struggle to strike a balance between the smoothness of ground-based movement and the ability to navigate rough terrains.

Furthermore, when compared to certain terrestrial transformable robots like Passive Leg [31], T-shape [32], and Wheel Transformer [2], WSP-bot's obstacle-crossing performance is generally lower than these robots specifically designed for terrestrial locomotion. This is because the listed terrestrial mobile robots typically employ radial expansion to directly increase the spoke length, which significantly

*Table V. Characteristics of amphibious robots or similarly sized terrestrial mobile robots.*

Name	Mass (kg)	Size( $L \times W \times H$ ) (mm)	Max Speed (m/s)	Max Speed (bodylengths/s)	Obstacle-crossing ratio	Motion characteristics		
						Smoothness of wheeled motion	Obstacle-crossing capability	Aquatic mobility
WSP-bot	1.34	280 × 239 × 120	0.8 (on land) 0.26 (on water)	2.86 (on land) 0.93 (on water)	1.08	Y	Y	Y
AQUA	16	650 × 450 × 130	1 (under water)	1.54 (under water)	–	N	Y	Y
Ninja Legs	16-18	–	0.9 (on land)	–	–	N	Y	Y
AmphiHex-I	14.2	844 × 669 × 228	0.55 (on land) 0.42 (under water)	0.65 (on land) 0.5 (under water)	–	N	Y	Y
AmphiSTAR	0.246	265 × - × -	3.6 (on land) 1.5 (on water)	13.6 (on land) 5.66 (on water)	–	N	N	Y
Omni-Paddle	0.551	241 × 241 × 149	–	–	–	Y	N	Y
SHOALBOT	22	600 × 500 × 220	1.8 (on land) 1 (under water)	3 (on land) 1.67 (under water)	0.43	N	Y	Y
Passive Leg	1.23	304 × 304 × 118	–	–	–	Y	Y	N
T-shape	–	380 × 300 × 90	–	–	1.33	Y	Y	N
Wheel Transformer	0.7	340 × 210 × 80	0.8 (on land)	2.4 (on land)	1.53	Y	Y	N



raises the obstacle clearance height. In contrast, WSP-bot employs a radial folding approach to switch modes, keeping the spoke length unchanged. Despite a slightly lower obstacle-crossing ratio, this transformation method provides additional capability for aquatic movement and adaptability to transitioning between water and land environments.

## 6. Conclusion

This paper proposes a novel wheel-spoke-paddle transformable amphibious robot (WSP-bot) and conducts simulations and prototype experiments. The following conclusions can be drawn:

(1) The novel WSP-bot combines the stability and maneuverability of wheeled robots with the obstacle-crossing ability of legged robots through WSP modules and transformation mechanism and simultaneously possesses the capability of surface propulsion in water. Based on this, the structural design and control system design of the robot have been carried out.

(2) Upon the foundation of WSP module, a comprehensive analysis has been conducted to evaluate the theoretical transformation torque, the locomotion, and obstacle-crossing capabilities of the robot in spoke mode. A dynamic transformation method has been proposed to reduce the actuation forces required for transformation. This approach effectively minimizes the workload on servo motors and decreases energy consumption.

(3) The feasibility of the transformation and obstacle-crossing is verified by simulation, and the WSP module is proved to generate sufficient propulsion force on the water surface.

(4) A prototype of the robot was fabricated using a combination of 3D printing and machining techniques, followed by terrestrial and aquatic experiments. In wheel mode on land, the robot can achieve a maximum speed of 0.8 m/s. In spoke mode, the robot is capable of stably overcoming obstacles 1.08 times its spoke length. In paddle mode on water, the robot can reach a propulsion speed of 0.26 m/s. The outdoor/field experiments also substantiate the effectiveness of the proposed wheel-spoke-paddle hybrid amphibious robot.

**Author contribution.** Yikai Ge conceived and designed the study, carried out structural design, theoretical analysis, simulation, and experiments. Feng Gao contributed to structural design and theoretical analysis. Weixing Chen contributed to structural design and is responsible for funding acquisition, resources, supervision. Yikai Ge and Feng Gao wrote the article. Weixing Chen is responsible for reviewing and editing.

**Financial support.** This study was supported by National Defense Basic Scientific Research Program of China (Grant No. JCKY2020203B039), Shanghai Jiao Tong University 2030 Initiative (Grant No. WH510363001-9), Shanghai Jiao Tong University Scientific and Technological Innovation Funds and National Natural Science Foundation of China (Grant No. 12121002).

**Competing interests.** The authors declare that they have no known competing financial interests or personal relationships that could have appeared to influence the work reported in this paper.

**Ethical approval.** Not applicable.

**Supplementary material.** The supplementary material for this article can be found at <http://doi.org/10.1017/S0263574723001716>.

## References

- [1] S. C. Chen, K. J. Huang, W. H. Chen, S. Y. Shen, C. H. Li and P. C. Lin, "Quattroped: A leg-wheel transformable robot," *IEEE/ASME Trans. Mechatron.* **19**(2), 730–742 (2014). doi:[10.1109/Tmech.2013.2253615](https://doi.org/10.1109/Tmech.2013.2253615).
- [2] Y. S. Kim, G. P. Jung, H. Kim, K. J. Cho and C. N. Chu, "Wheel transformer: A wheel-leg hybrid robot with passive transformable wheels," *IEEE Trans. Robot.* **30**(6), 1487–1498 (2014). doi:[10.1109/Tro.2014.2365651](https://doi.org/10.1109/Tro.2014.2365651).
- [3] X. L. Xie, F. Gao, C. Huang and W. Zeng, "Design and development of a new transformable wheel used in amphibious all-terrain vehicles (A-ATV)," *J. Terramech.* **69**, 45–61 (2017). doi:[10.1016/j.jterra.2016.11.001](https://doi.org/10.1016/j.jterra.2016.11.001).

- [4] P. Schoeneich, F. Rochat, O. T.-D. Nguyen, R. Moser and F. Mondada, "TRIPILLAR: A miniature magnetic caterpillar climbing robot with plane transition ability," *Robotica* **29**(7), 1075–1081 (2011). doi:[10.1017/S0263574711000257](https://doi.org/10.1017/S0263574711000257).
- [5] L. Bai, J. Guan, X. H. Chen, J. Z. Hou and W. B. Duan, "An optional passive/active transformable wheel-legged mobility concept for search and rescue robots," *Robot. Auton. Syst.* **107**, 145–155 (2018). doi:[10.1016/j.robot.2018.06.005](https://doi.org/10.1016/j.robot.2018.06.005).
- [6] A. Bhole, S. H. Turlapati, R. V.S., J. Dixit, S. V. Shah and K. M. Krishna, "Design of a robust stair-climbing compliant modular robot to tackle overhang on stairs," *Robotica* **37**(3), 428–444 (2018). doi:[10.1017/S0263574718001108](https://doi.org/10.1017/S0263574718001108).
- [7] M. Russo and M. Ceccarelli, "A survey on mechanical solutions for hybrid mobile robots," *Robotics* **9**(2), (2020). doi:[10.3390/robotics9020032](https://doi.org/10.3390/robotics9020032).
- [8] M. Rafeeq, S. F. Toha, S. Ahmad and M. A. Razib, "Locomotion strategies for amphibious robots-A review," *IEEE Access* **9**, 26323–26342 (2021). doi:[10.1109/Access.2021.3057406](https://doi.org/10.1109/Access.2021.3057406).
- [9] A. Crespi and A. J. Ijspeert, "Online optimization of swimming and crawling in an amphibious snake robot," *IEEE Trans. Robot.* **24**(1), 75–87 (2008). doi:[10.1109/Tro.2008.915426](https://doi.org/10.1109/Tro.2008.915426).
- [10] A. Crespi, K. Karakasiliotis, A. Guignard and A. J. Ijspeert, "Salamandra robotica II: An amphibious robot to study salamander-like swimming and walking gaits," *IEEE Trans. Robot.* **29**(2), 308–320 (2013). doi:[10.1109/Tro.2012.2234311](https://doi.org/10.1109/Tro.2012.2234311).
- [11] K. Tadakuma, R. Tadakuma, M. Aigo, M. Shimojo, M. Higashimori, M. Kaneko, "'Omni-Paddle': Amphibious Spherical Rotary Paddle Mechanism," *IEEE International Conference on Robotics and Automation (ICRA)* (2011).
- [12] J. Z. Yu, R. Ding, Q. H. Yang, M. Tan, W. B. Wang and J. W. Zhang, "On a bio-inspired amphibious robot capable of multimodal motion," *IEEE/ASME Trans. Mechatron.* **17**(5), 847–856 (2012). doi:[10.1109/Tmech.2011.2132732](https://doi.org/10.1109/Tmech.2011.2132732).
- [13] J. Z. Yu, R. Ding, Q. H. Yang, M. Tan and J. W. Zhang, "Amphibious pattern design of a robotic fish with wheel-propeller-fin mechanisms," *J. Field Robot.* **30**(5), 702–716 (2013). doi:[10.1002/rob.21470](https://doi.org/10.1002/rob.21470).
- [14] Y. Yang, G. Zhou, J. Zhang, S. Cheng, M. Fu and Ieee, "Design, Modeling and Control of A Novel Amphibious Robot with Dual-Swing-Legs Propulsion Mechanism," *IEEE/RSJ International Conference on Intelligent Robots and Systems (IROS)* (2015) pp. 559–566.
- [15] L. Bruzzone and G. Quaglia, "Review article: Locomotion systems for ground mobile robots in unstructured environments," *Mech. Sci.* **3**(2), 49–62 (2012). doi:[10.5194/ms-3-49-2012](https://doi.org/10.5194/ms-3-49-2012).
- [16] A. S. Boxerbaum, P. Werk, R. D. Quinn, R. Vaidyanathan and Ieee, "Design of an Autonomous Amphibious Robot for Surf Zone Operation: Part I - Mechanical Design for Multi-Mode Mobility," *IEEE/ASME International Conference on Advanced Intelligent Mechatronics* (2005) pp. 1459–1464.
- [17] R. Harkins, J. Ward, R. Vaidyanathan, A. S. Boxerbaum, R. D. Quinn and Ieee, "Design of an Autonomous Amphibious Robot for Surf Zone Operations: Part II - Hardware, Control Implementation and Simulation," *IEEE/ASME International Conference on Advanced Intelligent Mechatronics* (2005) pp. 1465–1470.
- [18] R. Altendorfer, N. Moore, H. Komsuoglu, M. Buehler, H.B. Brown Jr., D. McMordie, U. Saranli, R. Full and D.E. Koditschek, "RHex: A biologically inspired hexapod runner," *Auton. Robot.* **11**(3), 207–213 (2001). doi:[10.1023/A:1012426720699](https://doi.org/10.1023/A:1012426720699).
- [19] U. Saranli, M. Buehler and D. E. Koditschek, "RHex: A simple and highly mobile hexapod robot," *Int. J. Robot. Res.* **20**(7), 616–631 (2001). doi:[10.1177/02783640122067570](https://doi.org/10.1177/02783640122067570).
- [20] L. Pei-Chun, H. Komsuoglu and D. E. Koditschek, "Sensor data fusion for body state estimation in a hexapod robot with dynamical gaits," *IEEE Trans. Robot.* **22**(5), 932–943 (2006). doi:[10.1109/tro.2006.878954](https://doi.org/10.1109/tro.2006.878954).
- [21] J. C. Spagna, D. I. Goldman, P. C. Lin, D. E. Koditschek and R. J. Full, "Distributed mechanical feedback in arthropods and robots simplifies control of rapid running on challenging terrain," *Bioinspir. Biomim.* **2**(1), 9–18 (2007). doi:[10.1088/1748-3182/2/1/002](https://doi.org/10.1088/1748-3182/2/1/002).
- [22] X. G. Song, X. L. Zhang, X. Y. Meng, C. J. Chen and D. S. Huang, "Gait optimization of step climbing for a hexapod robot," *J. Field Robot.* **39**(1), 55–68 (2022). doi:[10.1002/rob.22037](https://doi.org/10.1002/rob.22037).
- [23] G. Dudek, P. Giguere, C. Prahacs, S. Saunderson, J. Sattar, L. A. Torres-Mendez, M. Jenkin, A. German, A. Hogue, A. Ripsman, J. Zacher, E. Milios, H. Liu, P. Zhang, M. Buehler and C. Georgiades, "AQUA: An amphibious autonomous robot," *Computer* **40**(1), 46–53 (2007). doi:[10.1109/Mc.2007.6](https://doi.org/10.1109/Mc.2007.6).
- [24] B. B. Dey, S. Manjanna and G. Dudek, "Ninja Legs: Amphibious One Degree of Freedom Robotic Legs," *IEEE/RSJ International Conference on Intelligent Robots and Systems (IROS)* (2013) pp. 5622–5628.
- [25] F. Zhou, X. Xu, H. Xu, Y. Chang, Q. Wang and J. Chen, "Implementation of a reconfigurable robot to achieve multimodal locomotion based on three rules of configuration," *Robotica* **38**(8), 1478–1494 (2019). doi:[10.1017/S0263574719001589](https://doi.org/10.1017/S0263574719001589).
- [26] Z. R. Luo, J. Z. Shang, G. W. Wei and L. Ren, "A reconfigurable hybrid wheel-track mobile robot based on Watt II six-bar linkage," *Mech. Mach. Theory* **128**, 16–32 (2018). doi:[10.1016/j.mechmachtheory.2018.04.020](https://doi.org/10.1016/j.mechmachtheory.2018.04.020).
- [27] Y. Sun and S. G. Ma, "A versatile locomotion mechanism for amphibious robots: Eccentric paddle mechanism," *Adv. Robot.* **27**(8), 611–625 (2013). doi:[10.1080/01691864.2013.763750](https://doi.org/10.1080/01691864.2013.763750).
- [28] S. W. Zhang, X. Liang, L. C. Xu and M. Xu, "Initial development of a novel amphibious robot with transformable fin-leg composite propulsion mechanisms," *J. Bionic Eng.* **10**(4), 434–445 (2013). doi:[10.1016/S1672-6529\(13\)60247-4](https://doi.org/10.1016/S1672-6529(13)60247-4).
- [29] S. W. Zhang, Y. C. Zhou, M. Xu, X. Liang, J. M. Liu and J. Yang, "AmphiHex-I: Locomotory performance in amphibious environments with specially designed transformable flipper legs," *IEEE/ASME Trans. Mechatron.* **21**(3), 1720–1731 (2016). doi:[10.1109/Tmech.2015.2490074](https://doi.org/10.1109/Tmech.2015.2490074).
- [30] X. M. Ma, G. Wang and K. X. Liu, "Design and optimization of a multimode amphibious robot with propeller-leg," *IEEE Trans. Robot.* **38**(6), 3807–3820 (2022). doi:[10.1109/Tro.2022.3182880](https://doi.org/10.1109/Tro.2022.3182880).
- [31] Y. She, C. J. Hurd, H.-J. Su and Ieee, "A Transformable Wheel Robot with A Passive Leg," *IEEE/RSJ International Conference on Intelligent Robots and Systems (IROS)* (2015) pp. 4165–4170.

[32] T. Sun, X. Xiang, W. H. Su, H. Wu and Y. M. Song, "A transformable wheel-legged mobile robot: Design, analysis and experiment," *Robot. Auton. Syst.* **98**, 30–41 (2017). doi:[10.1016/j.robot.2017.09.008](https://doi.org/10.1016/j.robot.2017.09.008).

### Appendix

Eight stages during obstacle-crossing with obstacle height  $H=60$  mm:

$$\begin{aligned}
 \text{Stage1: } & \begin{cases} X_{p1} = R_s \cos(\omega t) \\ X_{p2} = 0 \\ \theta = \arcsin\left(\frac{R_s \sin(\omega t)}{L}\right) \end{cases} \quad \left(0 \leq t \leq \frac{\beta}{\omega}\right), \\
 \text{Stage2: } & \begin{cases} X_{p1} = R_s \cos(\omega t) \\ X_{p2} = -R_s \sin(\omega t - \beta) \\ \theta = \arcsin\left(\frac{R_s \sin(\omega t) + H - R \cos(\omega t - \beta)}{L}\right) \end{cases} \quad \left(\frac{\beta}{\omega} < t \leq \frac{\pi + 2\beta}{4\omega}\right), \\
 \text{Stage3: } & \begin{cases} X_{p1} = R_s \cos(\omega t) \\ X_{p2} = R_s \cos(\omega t) \\ \theta = \arcsin\left(\frac{H}{L}\right) \end{cases} \quad \left(\frac{\pi + 2\beta}{4\omega} < t \leq \frac{\pi}{2\omega}\right), \\
 \text{Stage4: } & \begin{cases} X_{p1} = 0 \\ X_{p2} = 0 \\ \theta = \arcsin\left(\frac{H}{L}\right) \end{cases} \quad \left(\frac{\pi}{2\omega} < t \leq \frac{\pi + 2\beta}{2\omega}\right), \\
 \text{Stage5: } & \begin{cases} X_{p1} = -R_s \sin\left(\omega t - \left(\frac{\pi}{2} + \beta\right)\right) \\ X_{p2} = -R_s \sin\left(\omega t - \left(\frac{\pi}{2} + \beta\right)\right) \\ \theta = \arcsin\left(\frac{H}{L}\right) \end{cases} \quad \left(\frac{\pi + 2\beta}{2\omega} < t \leq \frac{3\pi + \beta}{4\omega}\right), \\
 \text{Stage6: } & \begin{cases} X_{p1} = R_s \cos\left(\omega t - \frac{\pi}{2}\right) \\ X_{p2} = R_s \cos\left(\omega t - \frac{\pi}{2}\right) \\ \theta = \arcsin\left(\frac{H}{L}\right) \end{cases} \quad \left(\frac{3\pi + \beta}{4\omega} < t \leq \frac{\pi}{\omega}\right), \\
 \text{Stage7: } & \begin{cases} X_{p1} = 0 \\ X_{p2} = R_s \cos(\omega t - \pi) \\ \theta = \arcsin\left(\frac{R - R \sin(\omega t - \pi)}{L}\right) \end{cases} \quad \left(\frac{\pi}{\omega} < t \leq \frac{\pi + \beta}{\omega}\right), \\
 \text{Stage8: } & \begin{cases} X_{p1} = -R \sin(\omega t - (\pi + \beta)) \\ X_{p2} = R \cos(\omega t - (\pi + \beta)) \\ \theta = \arcsin\left(\frac{R \cos(\omega t - (\pi + \beta)) - R \sin(\omega t - (\pi + \beta))}{L}\right) \end{cases} \quad \left(\frac{\pi + \beta}{\omega} < t \leq \frac{5\pi + \beta}{\omega}\right).
 \end{aligned}$$